Variations of the Martian plasma environment during the ICME passage on 8 March 2015 – A time-dependent MHD study

Y. J. Ma[1], C. T. Russell[1], X. Fang[2], C. F. Dong[3], A. F. Nagy[4], G. Toth[4], J. S. Halekas[5], J. E. P. Connerney[6], J. R. Espley[6], P. R. Mahaffy[6], M. Benna[6], J. McFadden[7], D. Mitchell[7], L. Andersson[2], and B. M. Jakosky[3]

[1]Department of Earth Planetary and Space Sciences, UCLA, Los Angeles, CA, USA

[2]Laboratory for Atmospheric and Space Physics, University of Colorado, Boulder, CO, USA

[3]Department of Astrophysical Sciences and Princeton Plasma Physics Laboratory, Princeton University, Princeton, NJ, USA

[4]Department of Atmospheric, Oceanic and Space Sciences, University of Michigan, Ann Arbor, MI, USA

[5]Department of Physics and Astronomy, University of Iowa, Iowa City, IA, USA

[6]NASA Goddard Space Flight Center, Greenbelt, MD, USA

[7]Space Sciences Laboratory, University of California, Berkeley, California, USA

Key points:

1. A time-dependent MHD model is used to quantify the impact of a strong ICME on Mars.
2. Plasma environment varied rapidly in response to the solar wind disturbances.

This is the author manuscript accepted for publication and has undergone full peer review but has not been through the copyediting, typesetting, pagination and proofreading process, which may lead to differences between this version and the Version of Record. Please cite this article as doi: 10.1002/2016JA023402

3. Ion escape rates were enhanced by more than an order of magnitude during the ICME event.

Abstract

The Mars Atmosphere and Volatile EvolutioN (MAVEN) spacecraft observed a strong interplanetary coronal mass ejection (ICME) impacting Mars on 8 March 2015. We use a time-dependent global MHD model to investigate the response of the Martian ionosphere and induced magnetosphere to the large solar wind disturbance associated with the ICME. Taking observed upstream solar wind conditions from MAVEN as inputs to the MHD model, the variations of the Martian plasma environments are simulated realistically in a time period from 2.5 hours prior to the arrival of the ICME shock to about twelve hours after the impact. Detailed comparisons between the model results and the relevant MAVEN plasma measurements are presented, which clearly show that the time-dependent multi-species single-fluid MHD model is able to reproduce the main features observed by the spacecraft during the ICME passage. Model results suggest that the induced magnetosphere responds to solar wind variation on a very short time scale (~ minutes). The variations of the plasma boundaries' distances from the planet along the subsolar line are examined in detail, which show a clear anti-correlation with the magnetosonic Mach number. Plasma properties in the ionosphere (especially the induced magnetic field) varied rapidly with solar wind changes. Model results also show that ion escape rates could be enhanced by an order of magnitude in response to the high solar wind dynamic pressure during the ICME event.

1. Introduction

ICMEs, as the interplanetary counterpart of coronal mass ejections (CMEs), often consist of several parts: a leading sheath-like pileup of solar-wind plasma and magnetic field sometimes preceded by a forward shock and a driver or ejecta portion [*Jian et al.*, 2008]. ICMEs are recognized as large-scale magnetic structures with enhanced field strength with respect to the ambient solar wind, having plasma and composition signatures distinct from the solar wind in which they are embedded [*Gopalswamy*, 2006]. It is well established that ICMEs are the main source of major geomagnetic storms observed at Earth [*Gosling et al.*, 1991; *Tsurutani and Gonzalez*, 1997]. Out of the ICME-perturbed solar wind, the high ram pressure and intense southward interplanetary magnetic field (IMF) are the most effective parameters causing large disturbances in the Earth's magnetosphere and ionosphere [*Cane et al.*, 2000; *Gonzalez et al.*, 2002; *Srivastava and Venkatakrishnan*, 2004].

Unlike Earth, unmagnetized planets interact with the impinging solar wind plasma much more directly. Intense solar wind disturbances like ICMEs are thus expected to play a more important role in controlling the nearby plasma environment. The increased atmospheric erosion by the ICME-induced solar wind disturbance is considered to be a matter of potential interest for historical extrapolation of atmospheric loss for unmagnetized planets [*Luhmann et al.*, 2008]. The importance of ICMEs to atmospheric erosion has been suggested based on the analysis of the data from both Pioneer Venus Orbiter (PVO) [*Luhmann et al.*, 2007] and Venus Express [*Edberg et al.*, 2011] for Venus and from Mars Express [*Edberg et al.*, 2010] for Mars. *Edberg* *et al.* [2011] suggested that the IMF polarity change across ICMEs could trigger dayside magnetic reconnections in the induced magnetosphere of Venus, which could add to the erosion through associated particle acceleration.

Several large ICME events at Mars (sometimes accompanied with other solar events such as solar energetic particle (SEP) and/or solar flares) were investigated from the observational point of view prior to the MAVEN era based on MGS or Mars Express data [*Crider et al.*, 2005; *Haider et al.*, 2009, *Opgenoorth et al.*, 2013, *Morgan et al.*, 2014]. However, these studies were restricted due to limited spacecraft coverage during those events or limited plasma instruments on board.

The Mars Atmosphere and Volatile EvolutioN (MAVEN) spacecraft was inserted into the Mars orbit in September 2014, with a comprehensive particle and field instrument package to measure the plasma environments around Mars [*Jakosky et al.*, 2015a]. MAVEN observed a strong interplanetary coronal mass ejection (ICME) impacting Mars around 8 March 2015. This event has been studied in detail by *Jakosky et al*. (2015b) using both MAVEN observations and three steady-state runs of a multi-species single-fluid MHD model. This event was also studied using a multi-fluid MHD approach for several stationary state runs [*Dong et al.*, 2015]. In addition, a strong magnetic flux rope was observed by MAVEN for a short time period during the event [*Hara et al.*, 2016]. Although the time-stationary results of the single-fluid and multi-fluid MHD models agree reasonably with MAVEN observations during most of the event [*Jakosky et al.*, 2015b, *Dong et al.*, 2015], they are unable to reproduce the observed variation of the magnetic field direction with time [*Jakosky et al.*, 2015b]. To quantify the dynamic response of the Martian plasma environment, a time-dependent global model is needed.

Time-dependent calculations have so far been limited due to the fact that they are computationally expensive. They have only been used to investigate the effect of the rotating crustal magnetic field under quiet solar wind conditions field [*Ma et al.*, 2014a, 2015, Fang et al, 2015] and during the response of the ionosphere to solar wind variations using ideal cases, such as pressure enhancement [*Ma et al.*, 2014b] and IMF rotation [*Modolo et al.*, 2012]. These studies showed that the outer plasma boundaries (bow shock and induced magnetosphere boundary (IMB)) adapt rapidly to the solar wind pressure enhancements and IMF rotation. In addition, the time-dependent high pressure enhancement study suggested that the ionospheric escape rates do not correlate only with the simultaneous solar wind dynamic pressure, but also depend on the earlier solar wind conditions [*Ma et al.*, 2014b].

In this study, for the first time, we use a time-dependent global MHD model to investigate the response of the Martian ionosphere/magnetosphere to a real ICME event. The global MHD model used for the study and its specific setup are briefly described in the next section. A detailed comparison of MHD model results with relevant MAVEN plasma observations along the spacecraft orbit during the ICME event are shown in section 3. A discussion and summary are given in section 4.

2. Time-dependent Multi-Species Single-Fluid MHD Model

2.1 Model description

The Multi-Species Single-Fluid MHD model for Mars utilizes the BATS-R-US (Block Adaptive-Tree Solar-wind Roe-type Upwind Scheme) code [*Powell et al.*, 1999; *Toth et al.*, 2012] from the University of Michigan. The model self-consistently calculates magnetic field, mass densities of protons and three ionospheric ion species (O^+, O_2^+ and CO_2^+), and mass averaged plasma velocity and temperature. A 3-D realistic ionosphere is constructed by considering major chemical reactions in the Mars ionosphere, including photo-ionization (mostly dayside) and electron impact ionization, charge exchange, and recombination reactions. The photoionization rates are calculated based on Chapman function [*Ma et al.*, 2015]. The effects of the crustal field anomalies are included using a 60-degree spherical harmonics model by Arkani-Hamed et al. [2001]. Early model results were mostly based on steady state simulations [Ma et al., 2002, 2004] with a certain crustal field configuration facing toward the Sun. The time-dependent MHD model has been recently applied to Mars and described in detail by *Ma et al.* [2014a, 2015]. In the time-dependent calculation, the rotation of the crustal anomalies is included with a realistic rotation period and tilt angle of Martian rotation axis.

The Mars-centered Solar Orbital (MSO) coordinate system (the X axis points from Mars to the Sun, the Y axis points antiparallel to Mars' orbital velocity, and the Z axis completes the right-hand system) is used in the calculation. The outer computational domain is given by: -8RT $\leq$ X $\leq$ 24RM , -16RM $\leq$ Y, Z $\leq$ 16RM. Such a large region ensures no artificial numerical effects from the outer boundary. A non-uniform spherical grid structure is used in the model, which allows a radial resolution that varies from 10 km (0.003R_M, where R_M= 3396 km) at the lower boundary to 480 km near the outer boundary in the distant tail. The angular resolution is 3 degrees in both longitudinal and latitudinal directions throughout the computation domain. Such a grid is the same as used in *Ma et al.* [2014b; 2015], so that the time-dependent calculation can be performed with reasonable computational resources. The inner boundary of the computational region is set to be 100 km above the surface of Mars, which is lower than the orbit periapsis altitude (~125-150 km) of MAVEN.

In the calculation, the neutral densities of CO_2, O and H are assumed to be spherically symmetric, and the altitude profiles and solar EUV strength are the same as used for the solar minimum conditions in *Ma et al.* [2004]. The rotational axis of Mars was set to be (-0.35, 0.24, 0.905), corresponding to the value in the middle of 8 March 2015. The simulation started from 12 UT in this day, which is roughly three hours before the leading ICME shock arrival at Mars, and the corresponding subsolar location is 97.4° E, 20.5° S. The season on Mars during that time was Southern Summer. The rotation of the crustal field is included in the model with a rotation period of 24 hours, 39 minutes and 57 seconds. Note that the position of the MAVEN trajectory is slightly adjusted by a small factor of 1.003 (=3396.0/3386.0) to get the correct altitude near periapsis. The model assumes a spherical body using the equatorial radius of 3396 km, which is about 10 km larger than the radius near periapsis.

2.2 Solar Wind Input of the Model during the March 8 ICME event

Figure 1 shows MAVEN plasma observations (solid lines) from the Solar Wind Ion Analyzer (SWIA) [*Halekas et al.*, 2015], the Solar Wind Electron Analyzer (SWEA) [*Mitchell et al.*, 2016], and the magnetometer (MAG) [*Connerney et al.*, 2015] instruments for the event. Panel (a) shows the altitude of the spacecraft varying from 158 km altitude at periapsis to 6233 km altitude at apoapsis. During the event, the MAVEN orbit was close to the terminator plane, with the dusk side of the orbit tilted slightly towards nightside. For each 4.5-hour orbit, MAVEN spent roughly 2/3 of the time in the southern hemisphere. The rest of the panels show proton density, ion and electron temperature, plasma velocity components and magnetic field components.

Prior to the ICME arrival, the solar wind conditions were relatively quiet, with a proton density of 1.8 cm^{-3}, flow speed of 505 km/s, and IMF magnitude of 5 nT at round 11:30 UT, 8 March 2015. The corresponding solar wind dynamic pressure is 0.9 nPa [*Jakosky et al.*, 2015b]. The ICME shock arrived at Mars around 15:23 UT, as indicated by MAG data, with a strong enhancement and rotation of the magnetic field when MAVEN was located inside the Martian magnetosheath region, as shown by the vertical orange line. The disturbance lasted about 40 hours associated with a fast and dense solar wind flow. The bow shock crossings are marked by dark blue vertical lines with dash-dotted lines for outbound shock crossings and dotted lines for inbound crossings. Between the two lines are the time periods when MAVEN was in the solar wind. The average solar wind conditions during the four consecutive orbits were summarized in Table 1 of *Dong et al.* [2015] as the inputs to their steady state cases. In this study, we started the simulation from 12 UT and ran it for 15 hours, which covers the period from 2.5 hours before the ICME shock to more than a half day after the shock arrival.

To model the response of the Mars plasma environment to the ICME event, a realistic solar wind input condition is needed to drive the model. The solar wind input condition for the time-dependent MHD model is shown by the dashed lines in Figure 1. It was set up based on one-minute average MAVEN observations using the following approach: For the time periods when MAVEN was outside of the bow shock, if SWIA was in the solar wind mode, we used SWIA observations for solar wind density, velocity and proton temperature. One of the underlying assumptions for the MHD model is charge quasi-neutrality, so that $n_e = n_i$ (where n_e is the electron number density and n_i is the total ion density). For the single-fluid MHD model, the actual input temperature needed is the solar wind plasma temperature ($T_P = T_i + T_e$), and it was set as the sum of the SWIA proton ion temperature and the SWEA electron temperature, when both measurements were available. One-minute averaged MAG observations were used for the

IMF. When MAVEN was inside the shock, no direct solar wind measurement was available, thus we simply assume that solar wind conditions changed linearly from inbound to outbound values, except at the time of the ICME arrival. An arbitrary jump condition is set to mimic the drastic solar wind condition change upon the ICME shock arrival. Prior to 15:22 UT, the solar wind input is set to be the same as inbound condition (n_{sw}=1.9 cm^{-3}, Ux= -510 km/s, B =(-2.2, 3.2, -1.3) nT), and it changes to the outbound condition (n_{sw}=2.5 cm^{-3}, Ux= -700 km/s, B =(8.6, 0.4, -9.9) nT) in one minute at 15:23 UT, as shown in Figure 1 around the orange vertical line. The ICME shock is assumed as a planar structure that propagates into the simulation domain along the X-axis from the upstream boundary (X=-8 R_M). It takes roughly one minute for the structure to arrive at the planet, considering the fact that the solar wind flow speed was between 500 and 700 km/s.

3. MHD Model Results and Comparison with MAVEN Observations

3.1 Comparison with MAVEN plasma observations

Figure 2 shows the comparison of the model results with MAVEN observations along the orbit of the spacecraft. Plasma and field observations are plotted in solid lines, and the model results are plotted in dashed lines. The first panel is the same as in Figure 1, which shows the altitude of the spacecraft. Comparison of various plasma densities is shown in the second panel. Langmuir Probe and Waves (LPW) observations [*Andersson* et al., 2015] are plotted in blue, SWEA electron density in orange, SWIA H^+ density in black, and NGIMS O_2^+ density in red.

Corresponding MHD model results are plotted in dashed lines. The SupraThermal And Thermal Ion Composition (STATIC) [*McFadden et al.*, 2015] ion density data is not shown due to the “ion suppression” issue at the time period, which affect STATIC’s ability in obtaining the right ion density for low-energy ions (<10 eV) due to exposure to atomic oxygen. It is also worth noting that NGIMS only measures ion density every other orbit during the events. MHD-modeled total electron density is plotted with a blue dashed line, which matches well the LPW observations near periapsis. In locations farther away from the planet, where the plasma predominantly consists of protons, model results of electron number density and proton density are similar to each other and agree well with SWEA and SWIA observations. The MHD-modeled O_2^+ density agrees well with NGIMS O_2^+ density for the second periapsis, as shown in the figure (a more detailed comparison of ion densities near this periapsis is shown in section 3.4).

The third panel of Figure 2 shows a comparison of plasma temperatures. The electron temperature from LPW is shown in blue, electron temperature from SWEA in orange, H^+ temperature from SWIA in black and O_2^+ temperature from STATIC in red. The modeled plasma temperature is plotted with blue dashed line. Since we are using a single-fluid model, only one energy equation is solved for the total plasma temperature. The calculated temperature follows closely the proton temperature as measured by SWIA in most of the regions except near periapsis where electron temperature is higher than that of ions. This is because the plasma temperature is dominated by the ions in those regions. A more detailed comparison of ion temperatures near periapsis is shown in section 3.4.

The last two panels of Figure 2 show the comparison of plasma flow velocity and magnetic field vectors. The agreement is fairly good except for some limited regions. The bow shock crossing times as predicted by the MHD model are fairly close to the observed crossing times as marked by the dark blue vertical dashed lines. Across the shock, both model results and MAVEN observations show sharp changes in proton/electron density and temperature, direction and magnitude of flow velocity and magnetic field.

3.2 Interaction with the ICME shock

The March 8 ICME event was led by a strong shock that impacted Mars around 15:23 UT. When the shock arrived at Mars, MAVEN was inside the Martian dawn-side magnetosheath region, moving down from the equatorial plane. Plasma conditions changed abruptly with the ICME shock. The observed plasma after the ICME shock was hotter, denser and faster with stronger magnetic field strength and a different magnetic field orientation.

Figure 3 shows the variations of the plasma environments during the ICME shock passage from model calculations. The left and right panels correspond to contour plots of magnetic field strength and plasma flow speed respectively, at 4 different times from 15:22 UT to 15:25 UT.

The white lines in the left panels are the magnetic field traces in the the XY plane, and the white arrows in the right panels show the plasma flow direction. The top two panels correspond to 15:22 UT, right before ICME shock arrival. At this time, both the bow shock and the IMB locations are close to the mean boundaries from past observations [*Edberg et al.*, 2008]. The solar wind plasma flow slows down and diverts around the planet, while the magnetic field piles up and drapes around the obstacle. The ICME shock arrived at Mars around 15:23 UT with a much faster flow speed and a stronger IMF as shown in the second row. The two consecutive panels in the third row show that another minute later, the ICME shock front already passed Mars, reaching around 10 R_M downstream, and the plasma environment around the planet was significantly altered by the fast solar wind flow. Both the solar wind density and velocity after the ICME shock increased significantly, and the dynamic pressure rose from 0.9 nPa to 3.1nPa. As the IMF strength increased by more than a factor of 4 across the ICME shock, the magnetic field strength in the magnetosheath region was enhanced accordingly across the Martian bow shock. The field strength in the induced magnetosphere was also significantly enhanced, since most of the solar wind dynamic energy converted into the magnetic energy inside the region. The bow shock moved slightly outward due to the decrease of the fast magnetosonic Mach number (a detailed discussion of plasma boundaries is presented in next section). Also note that plasma boundaries were tilted toward dusk due to the large off-X-axis flow velocity (≈ 100 km/s) in +Y direction. At 15:25 UT, as shown in the bottom panels, the ICME shock passed way beyond Mars, and the outer interaction region already reached a quasi-steady state. It is also interesting to note that in the flank region just inside the IMB, the plasma flow is somewhat faster than the solar wind speed. This is likely due to the JxB force (the magnetic field is mainly in negative Z direction in this time), so the draped fields in the XZ plane would accelerate the plasma in the flank region. This does not show up in the normal solar wind condition, because the draped field is not as strong. These snapshots clearly show that both the magnetosheath region and induced magnetosphere adapt rapidly to variations in the solar wind.

3.3 Variation of the plasma boundaries

The top panel of Figure 4 shows the subsolar bow shock (BS) distance and the induced magnetospheric boundary (IMB) location from the MHD model as functions of time. Corresponding solar wind parameters were also plotted in the subsequent panels as references. During the simulated 15-hour time period, the BS location varied from 1.4 to 1.63 R_M, while the IMB location varied from 1.1 to 1.36 R_M. Here, the subsolar BS location is defined as the location where the plasma dynamic pressure is equal to the plasma thermal pressure, while the IMB is determined where the magnetic pressure is balanced by the plasma thermal pressure. The time periods when BS and IMB were farthest from the planet are shaded in red and blue, respectively. The model predicts that the maximum BS location occurred right after shock arrival ranging from 15:25 UT to 15:30 UT, and the maximum IMB took place at a similar but shorter time period from 15:25 UT to 15:27 UT. Even though, as discussed in the last section, the solar wind dynamic pressure (P_{SW}) was significantly enhanced after the ICME shock, the fast magnetosonic Mach number (Mf) actually decreased across the ICME shock, due to high plasma temperature and enhanced magnetic field strength. As a result, both the Alfven speed ($V_A = \frac{B}{\sqrt{\mu_0 \rho}}$) and sonic speed ($V_S = \sqrt{\frac{\gamma P}{\rho}}$, where P= nkT_P) significantly increased across the ICME shock as shown in the second-to-last panel. This is consistent with previous statistical results [*Edberg* et al., 2010] that the M_f is the main factor controlling the bow shock location. As the M_f dropped from 6.1 to 3.3 across the shock, both the BS location and IMB location moved farther away. The bow shock location then gradually decreased in response to the subsequent increase in Mf. However, when the Mf returned to 6.1 around 18:40 UT, the shock location was closer to the planet than that of the quiet conditions, because of the much higher solar wind dynamic pressure at the time. The model results clear show that the solar wind dynamic pressure controls the bow shock location as well.

The interaction region is significantly compressed later by the sheath plasma of the ICME as the Mf value gradually increased. The plasma boundaries came closest to Mars from 20:06 UT to 20:44 UT for BS and 20:20 UT to 20:42 UT for IMB, as shown by the shaded area (yellow for BS and green for IMB), when the M_f was close to its highest value (9.1). Interestingly, the highest M_f was associated with extremely high solar wind dynamic pressure (≈ 15 nPa). The subsolar BS and IMB locations are closely correlated, as clearly shown in the top panel of the figure. The ratio between BS and IMB distance ranges from 1.2 to 1.3 with a mean value of 1.25, which is likely modulated by the crustal magnetic field distribution in the subsolar region.

Figure 5 shows snapshots of the pressure profiles along the Mars-Sun line for a few representative times during the event. The first panel shows the pressure profiles at 12:00 UT, which is the start time of the simulation. The bow shock location was at 1.6 R_M and the IMB was around 1.28R_M. From the solar wind to the ionosphere, the dominant pressure changes from the solar wind dynamic pressure $P_{dynamic}$ (in the solar wind) to the plasma thermal pressure $P_{thermal}$ (in the magnetosheath region) to magnetic pressure P_B (inside the induced magnetosphere) and to crustal magnetic pressure P_{B0} (in the ionosphere). At this particular time, the low-altitude subsolar region is dominated by strong crustal magnetic fields with a peak value around 134 nT, thus the magnetic pressure ($\approx$ 7nPa) is much higher than the ionospheric thermal pressure in the ionosphere.

Panel (b) shows the pressure profiles at 15:22 UT, right before the ICME shock arrival. The solar wind condition at this time is quite close to that of 12:00 UT. The bow shock location was at 1.57 R_M, slightly closer to the planet as compared with panel (a), while the location of IMB was almost identical. At this time, the subsolar peak crustal magnetic field was about 37 nT, corresponding to a crustal magnetic pressure of 0.54 nPa, similar to the ionospheric thermal pressure. Panel (c) shows the pressure profiles at 15:23 UT, when the ICME shock arrived at Mars. At this time, the solar wind dynamic pressure was sharply enhanced by a factor of two, and as a result, the thermal pressure inside the magnetosheath region increased significantly almost instantly. The magnetic pressure in the magnetosheath region and induced magnetosphere was also enhanced in response. As it takes longer for the information of the solar wind to propagate into regions closer to the planet due to slowdown of the plasma flow, the induced magnetic field in the deep ionosphere was not affected. As a result, there is a local minimum forming in the magnetic pressure profile around 1.1 R_M. The plasma boundaries were pushed inward slightly by the high solar wind dynamic pressure at first, but those boundaries moved outward in response to the decrease of the fast magnetosonic number at 15:25 UT, as shown in panel (d).

The upstream solar wind dynamic pressure gradually increased at subsequent times, as shown at 16:00 UT and 18:00 UT, as did the thermal pressure of the shocked solar wind inside the magnetosheath region. The upstream solar wind dynamic pressure reached its maximum value 15 nPa around 20:30 UT, when the interaction region was mostly compressed by the fast flowing solar wind. The peak of the induced magnetic field at this time is about 186 nT, corresponding to 87% of the P_{SW} upstream. Around 23:00 UT, the solar wind dynamic pressure gradually dropped to a lower value as did the thermal pressure in the magnetosheath region and the magnetic pressure inside the IMB.

Figures 4 and 5 clearly show that the plasma environments around Mars were highly variable during the ICME event. It is also worth noting that the ionosphere was magnetized either by the induced magnetic field or crustal magnetic field during the whole event, since the upstream solar wind pressure dominates over the ionospheric thermal pressure.

3.4 Variation of the ionosphere

To illustrate how the ionosphere responded to the large solar wind disturbance associated with the ICME, we compare various plasma properties along the subsolar line at different times in Figure 6. Those snapshots correspond to the same times shown in Figure 5. The top three panels (a1-a3) show the results at 12:00 UT when the solar wind condition was relatively quiet. Panel (a1) shows profiles of number densities of different ion species and electrons from 100 – 1000-km altitude. The modeled ionosphere was mainly composed of O_2^+ in the ionosphere below 400 km altitude, and H^+ became the dominant ion at higher altitudes. Panel (a2) shows altitude profiles of the three components of the induced magnetic field (solid lines) and the crustal magnetic field (dotted lines). The total magnetic field is the sum of the crustal magnetic field and the induced magnetic field; the latter is the perturbation of the magnetic field induced by the solar wind interaction. The induced magnetic field components drop to zero at 100 km altitude because we force the total magnetic field at the inner boundary to be the same as the local crustal field. At high altitudes, the total magnetic field was mainly contributed by the induced magnetic field, with its direction controlled by the IMF orientation. Below 300-km altitude, the crustal magnetic field became dominant. At this particular time, the crustal field was very strong, especially in the +Y direction with a peak value of 110 nT near the inner boundary. Panel (a3) shows profiles of plasma velocity components. The shocked solar wind flow continued to move down toward the planet at around 1000 km altitude at a speed of 30 km/s, as shown by the negative U_X component. The plasma flow speed gradually dropped with decreasing altitude, and became nearly stagnant below 450 km altitude. Previous model results showed that the plasma flow along the subsolar line only moved along the X direction when the crustal magnetic field is not included in the calculation [*Ma et al.*, 2014]. The significant flow along the Y and Z directions in panel (a3) was caused by the strong non-uniform crustal magnetic field in the subsolar region.

At 15:22 UT, density profiles were essentially not affected below 200 km altitude, because the plasma densities are mainly controlled by photo-chemical reactions in the collision-dominant region. All the ion densities increased slightly between 200 km and 800 km altitude in comparison with the values at 12:00 UT (the dashed lines), as shown in panel (b1). The solar wind condition at this time was quite similar to 12:00 UT, while the subsolar crustal magnetic field was much weaker. Stronger induced magnetic fields were formed to help slow down the impinging plasma flow as shown in panel (b2). Compared with the prior time, the plasma flow in the X-direction was reduced to zero at higher altitude (panel b3) due to the stronger total magnetic fields above 450 km altitude, which is the main reason for the expansion of the ionosphere.

At 15:23 UT, the densities of planetary ions (O^+, O_2^+ and CO_2^+) all decreased between 300 and 600 km altitudes (panel c1). The induced magnetic fields above 250 km altitude changed drastically, compared to just one minute before, forming a sharp discontinuity in the B_Y profile in the ionosphere. This was also associated with plasma flow moving downward at a finite speed of a few km/s. As discussed in the previous section, at this time, the solar wind dynamic pressure was sharply enhanced by a factor of two, which pushed the plasma boundaries inward and compressed the ionosphere.

At 15:25 UT, the variation of different ions became complicated and showed different behavior. The densities of O_2^+ and CO_2^+ in the lower altitude region continued decreasing, but became denser at higher altitudes. The density of O^+ increased above 250 km altitude. The induced magnetic field changed significantly from the prior time. As the upstream IMF direction changed from mainly B_Y to B_Z, in association with the ICME leading shock, there is a large induced magnetic field in B_Z component that formed correspondingly and propagated to low altitudes. There was also a large flow in both Y and Z directions, as shown in panel (d3), partly due to the large off-X-axis solar wind flow upstream.

After the shock, the solar wind density and dynamic pressure gradually increased, and the total magnetic field was dominated by the induced magnetic field. The peak values of the induced magnetic field increased from 87 nT at 16:00 UT to 147 nT at 18:00 UT to 186 nT at 20:30 UT in response to the enhancement of the solar wind dynamic pressure. The main induced magnetic field component changed from the B_Y to B_Z component in response to the clock angle change of the IMF. The plasma flow penetrated to a lower altitude in comparison to before, and the ionosphere was significantly compressed. The induced magnetic field in the Y direction changed from positive to negative and then positive again during this time period in response to variations of the upstream IMF. At 23:00 UT, the solar wind proton density decreased from its peak value, and as a result, the induced magnetic field decreased and was dominated by the positive B_Y component again.

Figure 7 shows a comparison of model results and MAVEN observations near periapsis of orbit 848. This is the first periapsis after the ICME shock arrival. MAVEN was moving from the dayside ionosphere to the nightside, and the periapsis corresponded to 80 degrees SZA (Solar Zenith Angle) and 16 UT local time. The modeled densities have similar trends as the observations but are about 3 times smaller than the observations. The discrepancy is mainly because the neutral atmosphere and solar EUV flux used in the model are for solar minimum conditions. Such a condition was selected in the simulation because previous model results suggested that this condition matched well with NGIMS observations [*Jakosky et al.,* 2015b, *Dong et al.*, 2015]. However, the recently available LPW data and the new calibration of NGIMS suggested that the plasma density is about a factor 3 larger than previously calibrated NGIMS values. The agreement is somewhat better during the outbound part of the trajectory. The plasma temperature calculated by the model is consistent with LPW measurements of the electron temperature, which is about 3 times higher than the ion temperature near periapsis. The crustal magnetic field near the closest approach is about 30 nT, slightly smaller than the induced magnetic field. The calculated magnetic field profiles are in good agreement with observation near periapsis.

3.5 Variation of the ion loss rate

Figure 8 shows the variation of the integrated ion escape rates during the ICME event. Here the escape rates are estimated by integrating over R= 6 R_M sphere of the plasma flux in radial direction (plasma density times the radial velocity) for each ion species. For the majority of the time simulated, O_2^+ was the main ion species escaping from the planet. The ion loss rates are positively related to the solar wind dynamic pressure. The peak ion loss rate occurred around the same time as the peak solar wind dynamic pressure at 20:44 UT, and the corresponding ion loss rates were enhanced by nearly an order of magnitude. As a comparison, the solar wind dynamic pressure was about 20 times larger than that at quiet conditions. The escaping O^+ ions became comparable or even dominant during a short period of time when the solar wind density and pressure were around the highest during this period. This can be explained by the enhancement of the charge exchange reaction between H^+ and O associated with the increase in the solar wind proton density at the time period, as shown in panel(g1) of Figure 6, thus the O^+ density became larger than O_2^+ at high altitude around this time and contributed the most to the total ion loss. As both the neutral atmosphere and EUV flux are kept constant in the model, the only change around 21:00UT to 22:00 UT is the enhancement of the solar wind proton density. A rough estimate shows that the charge exchange reaction rate (~ 3×10^{-7} s^{-1}) between 200-300 km altitude is more than twice larger than the un-attenuated photoionization rate (1.2×10^{-7} s^{-1}) of oxygen atoms.

Also plotted in Figure 8 are the escape rates based on three steady-state simulations (marked by symbols), and the results are quite different from the time-dependent model results. Note that these steady-state runs corresponded to the crustal field configuration near periapsis, while the solar wind conditions were based on the mean MAVEN solar wind observations before inbound shock crossings. The peak ion loss rates for the steady state cases are about 25- 30 percent larger than the peak ion loss rates predicted by the time-dependent simulation. As the steady-state runs could not take into account the response time of the system or the rotation of the crustal field, the escape rates as predicted by the time-dependent MHD model are more credible. The difference shows clearly that the system does not reach steady-state conditions right away. As suggested by *Ma et al*. [2014a) and *Fang et al*. [2015], the heavier ions have larger variation with the crustal field rotation than the light ion (O^+), and the response time could be 2-3 hours for heavy ions. It is suggested that the time-varying solar wind conditions and the continuously rotating crustal field work together to control the total ion escape rate, thus a time-dependent simulation is more appropriate to quantify the ion loss rates.

4. Discussion and Summary

This is the first time a time-dependent study of a real ICME event was carried out for Mars. In the study, the impact of a strong ICME on Mars was modeled using the observed solar wind conditions during the event. Through detailed comparison with relevant MAVEN plasma observations along the orbit, we find that in general, the time-dependent multi-species single-fluid MHD model reproduced well the main features that were observed by the spacecraft during the ICME passage.

Model results show that plasma boundaries were highly variable during the event and the boundary locations were mainly controlled by the fast magnetosonic Mach number (Mf). In addition, solar wind dynamic pressure also has some influence on the bow shock locations. We find that higher solar wind dynamic pressure results in closer distances of the boundaries for similar Mf. Plasma properties in the ionosphere and the induced magnetosphere varied significantly in response to the disturbance in the solar wind. Along the subsolar line, the peak value of the magnetic pressure in the induced magnetosphere is about the same as the normal of the solar wind dynamic pressure most of the time, when the corresponding crustal magnetic field is weak. The main component of the magnetic field in the ionosphere is the same as that of the IMF.

As Mars rotates, the part of the non-uniform crustal field that interacts with the solar wind also varies. It is apparent that the crustal field plays some important role in the interaction process. Sometimes, it is hard to distinguish whether the upstream solar wind or the rotating crustal field is the main driver of the variation seen in the Martian plasma environment. Comparison with the steady-state solution of the model clearly demonstrated that the system needs time to respond to both external and internal driving forces. Model results show that ion escape rates could be an order of magnitude enhanced in response to the high solar wind dynamic pressure during the ICME event. The continuously rotating crustal field also contributes to some variations of the total ion escape rates. Model results suggest that different ion species respond differently to the two drivers. The heavier ions have larger variation with the crustal field rotation than the light ion (O^+), while O^+ has a larger dependence on the solar wind proton density. Simulations results show that O^+ escape dominates when solar wind proton density is significantly high.

The model predicts that the total ion loss rate would be enhanced by an order of magnitude during the event for a short period of time. Even though this enhancement might not seem to be large enough for the solar-wind driving ion loss to be the dominate escape channel, we should keep in mind that, for early Mars, in addition to the larger solar wind density and velocity [*Wood et al.*, 2005], the EUV flux was also expected to be much stronger [*Ribas et al.*, 2005], which is not included in this event study. Previous observation and numerical studies showed that EUV flux also has significant effect on ion loss rate [*Ma et al.*, 2007, *Lundin et al.*, 2013, *Dong et al.*, 2014]. The escape rate calculated for this particular event should only be taken as a lower limit of the escape rate for early Mars.

The present model uses a spherical symmetric neutral atmosphere, thus both the noon-midnight and dawn-dusk asymmetry were neglected in the calculation. The solar wind interaction can therefore be expected to be more asymmetric than what the model predicts. This could partly explain the more symmetric model result around periapsis in Figure 7b compared to the asymmetric observed densities. The model predicted that O_2^+ dominated near periapsis along the MAVEN orbit (until H^+ is dominates), while NGIMS observations show that during the outbound pass, the heavy ion density drops off rapidly above 280 km altitude, and the ionosphere is dominated by O^+ (Figure 7b) for a short time period around 18:00 UT. The discrepancy is likely due to kinetic effects (for example ion heating due to plasma waves, as suggested by *Andersson et al.* [2010]) that were neglected in the single-fluid MHD model. Also, keep in mind that the absolute values of different ions and thus exact ratios between O^+/O_2+ presented in Figure 8 could be influenced by the neutral atmosphere input of the model and the EUV conditions. To further improve the fit to data and to provide a better estimate of the ion escape rates, the model needs to update its neutral profiles based on MAVEN observations, and photo-ionization rates from the measured solar EUV spectra. In addition, the atmosphere would also respond to the ICME-associated energetic pick-up ion precipitation [*Fang et al.*, 2013]. Since the solar wind had high density, velocity and temperature, more ions would be picked up by the solar wind with higher energy, thus more energy would be deposited into the neutral. The atmospheric response under extreme conditions includes neutral temperature enhancement, significant neutral composition and wind changes. Such effects are not considered in the present study, as the neutral atmosphere is preset in the MHD model. We do plan in the future to include the variations of the neutral atmosphere in the model through a two-way coupled approach.

Solar flare events were also observed before the ICME arrival and were likely related to the major interplanetary disturbance of this period. In the present study, we mainly focused on the variations of the solar wind plasma and their corresponding ionospheric responses; effects of solar flares on ionosphere have also been observed and investigated [*Futaana et al*., 2008, *Fallows et al*., 2015], and their global consequence is a good subject of future numerical studies.

Acknowledgments.

The work presented here was supported by NASA Grants NNX13AO31G. C. F. Dong is supported by the NASA Living with a Star Jack Eddy Postdoctoral Fellowship Program, administered by the University Corporation for Atmospheric Research. Resources supporting this work were provided by the NASA High-End Computing (HEC) Program through the NASA Advanced Supercomputing (NAS) Division at Ames Research Center. The MAVEN observational data used in the study were obtained from the NASA Planetary Data System (PDS). The Space Weather Modeling Framework that contains the BATS-R-US code used in this study

is publicly available from http://csem.engin.umich.edu/tools/swmf. For distribution of the model results used in this study, please contact the corresponding author.

References.

Andersson, L., R. E. Ergun, G. T. Delory, A. Eriksson, J. Westfall, H. Reed, J. McCauly, D. Summers, and D. Meyers (2015), The Langmuir probe and waves (LPW) instrument for MAVEN, *Space Sci. Rev.*, doi:10.1007/s11214-015-0194-3.

Andersson, L., R. E. Ergun, and A. I. F. Stewart (2010), The combined atmospheric photochemistry and ion tracing code: Reproducing the Viking Lander results and initial outflow results, Icarus, 206, 120–129, doi:10.1016/j.icarus.2009.07.009.

Arkani-Hamed, J. (2001), A 50-degree spherical harmonic model of the magnetic field of Mars, J. Geophys. Res., 106, 23,197–23,208.

Cane, H., I. Richardson, and O. Cyr, Coronal mass ejections, interplanetary ejecta, and geomagnetic storms, *Geophys. Res. Lett.*, *27*, 3591, 2000.

Connerney, J. E. P., J. R. Espley, P. Lawton, S. Murphy, J. Odom, R. Oliversen, and D. Sheppard (2015), The maven magnetic field investigation, Space Science Reviews, pp. 1–35, doi:10.1007/s11214-015-0169-4.

Crider, D. H., J. Espley, D. A. Brain, D. L. Mitchell, J. E. P. Connerney, and M. H. Acuña (2005), Mars Global Surveyor observations of the Halloween 2003 solar superstorm's encounter with Mars, J. Geophys. Res., 110, A09S21, doi:10.1029/2004JA010881.

Curry, S. M., J. G. Luhmann, Y. J. Ma, C. F. Dong, D. Brain, F. Leblanc, R. Modolo, Y. Dong, J. McFadden, J. Halekas, et al. (2015), Response of Mars O+ pickup ions to the 8 March 2015 ICME: Inferences from MAVEN data-based models, Geophys. Res. Lett., 42, 9095–9102, doi:10.1002/2015GL065304.

Dong, C., S. W. Bougher, Y. Ma, G. Tóth, A. F. Nagy, and D. Najib (2014), Solar wind interaction with Mars upper atmosphere: Results from the one-way coupling between the multifluid MHD model and the MTGCM model, *Geophys. Res. Lett.*, **41**, 2708–2715, doi:10.1002/2014GL059515.

Dong, C., Y. Ma, S. W. Bougher, G. Toth, A. F. Nagy, J. S. Halekas, Y. Dong, S.M. Curry, J. G. Luhmann, D. Brain, J. E. P. Connerney, J. Espley, P. Mahaffy, M. Benna, J. P. McFadden, D. L.

Mitchell, G. A. DiBraccio, R. J. Lillis, B. M. Jakosky, J. M. Grebowsky (2015), Multifluid MHD study of the solar wind interaction with Mars' upper atmosphere during the 2015 March 8th ICME event, *Geophys. Res. Lett.*, 42, doi: 10.1002/2015GL065944.

Edberg, N. J. T., M. Lester, S. W. H. Cowley, and A. I. Eriksson (2008), Statistical analysis of the location of the Martian magnetic pileup boundary and bow shock and the influence of crustal magnetic fields, J. Geophys. Res., 113, A08206, doi:10.1029/2008JA013096.

Edberg, N. J. T., M. Lester, S. W. H. Cowley, D. A. Brain, M. Fränz, and S. Barabash (2010), Magnetosonic Mach number effect of the position of the bow shock at Mars in comparison to Venus, J. Geophys. Res., 115, A07203, doi:10.1029/2009JA014998.

Edberg, N. J. T., et al. (2011), Atmospheric erosion of Venus during stormy space weather, J. Geophys. Res., 116, A09308, doi:10.1029/2011JA016749.

Ergun, R. E., et al. (2016), Enhanced O_2^+ loss at Mars due to an ambipolar electric field from electron heating, J. Geophys. Res. Space Physics, 121, 4668–4678, doi:10.1002/2016JA022349.

Fallows, K., P. Withers, and G. Gonzalez (2015), Response of the Mars ionosphere to solar flares: Analysis of MGS radio occultation data, J. Geophys. Res. Space Physics, 120, 9805–9825, doi:10.1002/2015JA021108.

Fang, X., Y. Ma, D. Brain, Y. Dong, and R. Lillis (2015), Control of Mars global atmospheric loss by the continuous rotation of the crustal magnetic field: A time-dependent MHD study, J. Geophys. Res. Space Physics, 120, 10,926–10,944, doi:10.1002/2015JA021605.

Gonzalez, W., B. Tsurutani, R. Lepping, and R. Schwenn (2002), Interplanetary phenomena associated with very intense geomagnetic storms, *J. Atmos. Solar-Terr. Phys., 64*, 173–181.

Gopalswamy, N. (2006), Properties of Interplanetary Coronal Mass Ejections. Space Sci. Rev, 124, 145 - 168. 10.1007/s11214-006-9102-1.

Gosling, J. T. (1997), *Coronal Mass Ejections*, in N. Crooker, J. A. Joselyn, and J. Feynman (eds.), AGU, Washington D.C., 9.

Gosling, J., D. McComas, J. Phillips, and S. Bame (1991), Geomagnetic Activity Associated with Earth Passage of Interplanetary Shock Disturbances and Coronal Mass Ejections, *J. Geophys. Res., 96*(A5), 7831–7839.

Haider, S. A., M. A. Abdu, I. S. Batista, J. H. Sobral, E. Kallio, W. C. Maguire, and M. I. Verigin (2009), On the responses to solar X-ray flare and coronal mass ejection in the ionospheres of Mars and Earth, *Geophys. Res. Lett., 36*, L13104, doi:10.1029/2009GL038694.

Halekas, J., E. Taylor, G. Dalton, G. Johnson, D. Curtis, J. McFadden, D. Mitchell, R. Lin, and B. Jakosky (2015), The solar wind ion analyzer for maven, Space Science Reviews, 195, pp. 125-151, doi:10.1007/s11214-013-0029-z.

Hara, T., J. G. Luhmann, J. S. Halekas, J. R. Espley, K. Seki, D. A. Brain, H. Hasegawa, J. P. McFadden, D. L. Mitchell, C. Mazelle, Y. Harada, R. Livi, G. A. DiBraccio, J. E. P. Connerney, L. Andersson, B. M. Jakosky (2016), MAVEN observations of magnetic flux ropes with a strong field amplitude in the Martian magnetosheath during the ICME passage on 8 March 2015, *Geophys. Res. Lett.*, 43, 4816-4824, doi:10.1002/2016GL068960.

Jakosky, B.M., Lin, R.P., Grebowsky, J.M. et al. (2015a), The mars atmosphere and volatile evolution (maven) mission, Space Sci Rev., 195: 3. doi:10.1007/s11214-015-0139-x.

Jakosky, B.M., et al (2015b), MAVEN observations of the response of Mars to an interplanetary coronal mass ejection, *Science* 350, DOI:10.1126/science.aad0210.

Jian, L.K., C.T. Russell, J.G. Luhmann et al. (2008), Stream Interactions and Interplanetary Coronal Mass Ejections at 5.3 AU near the Solar Ecliptic Plane, Sol Phys (2008) 250: 375. doi:10.1007/s11207-008-9204-x.

Luhmann, J. G., W. T. Kasprzak and C. T. Russell (2007), Space weather at Venus and its potential consequences for atmosphere evolution, J. Geophys. Res, 112, E04S10.

Luhmann, J. G. et al. (2008), Venus Express observations of atmospheric oxygen escape during the passage of several coronal mass ejections, J. Geophys. Res., 113, E00B04, doi:10.1029/2008JE003092.

Lundin, R., S. Barabash, M. Holmström, H. Nilsson, Y. Futaana, R. Ramstad, M. Yamauchi, E. Dubinin, and M. Fraenz (2013), Solar cycle effects on the ion escape from Mars, Geophys. Res. Lett., 40, 6028–6032, doi:10.1002/2013GL058154.

Ma, Y., A. F. Nagy, I. V. Sokolov, and K. C. Hansen (2004), Three-dimensional, multispecies, high spatial resolution MHD studies of the solar wind interaction with Mars, J. Geophys. Res., 109, A07211, doi:10.1029/2003JA010367.

Ma, Y.-J., and A. F. Nagy (2007), Ion escape fluxes from Mars, Geophys. Res. Lett., 34, L08201, doi:10.1029/2006GL029208.

Ma, Y., X. Fang, C. T. Russell, A. F. Nagy, G. Toth, J. G. Luhmann, D. A. Brain, and C. Dong (2014a), Effects of crustal field rotation on the solar wind plasma interaction with Mars, Geophys. Res. Lett., 41, 6563–6569, doi:10.1002/2014GL060785.

Ma, Y. J., X. Fang, A. F. Nagy, C. T. Russell, and G. Toth (2014b), Martian ionospheric responses to dynamic pressure enhancements in the solar wind, J. Geophys. Res. Space Physics, 119, 1272–1286, doi:10.1002/2013JA019402.

Ma, Y. J., C. T. Russell, X. Fang, Y. Dong, A. F. Nagy, G. Toth, J. S. Halekas, J. E. P. Connerney, J. R. Espley, P. R. Mahaffy, et al. (2015), MHD model results of solar wind interaction with Mars and comparison with MAVEN plasma observations, Geophys. Res. Lett., 42, 9113–9120, doi:10.1002/2015GL065218.

McFadden, J., O. Kortmann, G.J. Dalton, R. Abiad, D. Curtis, R. Sterling, K. Hatch, P. Berg, C. Tiu, M. Marckwordt, R. Lin, and B. Jakosky (2015), The MAVEN Suprathermal andthermal Ion Composition (STATIC) Instrument, Space Sci. Rev.

Mahaffy, P. R., et al. (2014), The Neutral Gas and Ion Mass Spectrometer on the Mars Atmosphere and Volatile Evolution mission, Space Sci. Rev., doi:10.1007/s11214-014-0091-1.

Modolo, R., G. M. Chanteur, and E. Dubinin (2012), Dynamic Martian magnetosphere: Transient twist induced by a rotation of the IMF, Geophys. Res. Lett., 39, L01106, doi:10.1029/2011GL049895.

Mitchell, D.L., C. Mazelle, J. Sauvaud, et al. (2016), The MAVEN Solar Wind Electron Analyzer, Space Sci. Rev., 200, 495-528, doi:10.1007/s11214-015-0232-1.

Morgan, D. D., et al. (2014), Effects of a strong ICME on the Martian ionosphere as detected by Mars Express and Mars Odyssey, J. Geophys. Res. Space Physics, 119, 5891–5908, doi:10.1002/2013JA019522.

Opgenoorth, H. J., D. J. Andrews, M. Fränz, M. Lester, N. J. T. Edberg, D. Morgan, F. Duru, O. Witasse, and A. O. Williams (2013), Mars ionospheric response to solar wind variability, J. Geophys. Res. Space Physics, 118, 6558–6587, doi:10.1002/jgra.50537.

Powell, K. G., P. L. Roe, T. J. Linde, T. I. Gombosi and D. L. DeZeeuw, (1999), A solution-adaptive upwind scheme for ideal magnetohydrodynamics, J. Comp. Phys., 154, 284.

Ribas et al., (2005), Evolution of the solar activity over time and effects on planetary atmospheres. I. High-energy irradiances (1 – 1700 Å), Astrophys. J., 622 (March) (2005), pp. 680 – 694.

Srivastava, N., and P. Venkatakrishnan (2004), Solar and interplanetary sources of major geomagnetic storms during 1996–2002, J. Geophys. Res., 109, A10103, doi:10.1029/2003JA010175.

Tsurutani, B. and W. Gonzalez (1997), The interplanetary causes of magnetic storms: A review, in *Magnetic Storms*, edited by B. Tsurutani, W. Gonzalez, Y. Kamide, and J. Arballo, *Geophys. Mon. Series, 98*, 77–89, Washington D. C..

Toth, G., et al. (2012), Adaptive numerical algorithms in space weather modeling, Journal of Computational Physics, 231, 3, 1 February 2012, 870-903, ISSN 0021-9991, 10.1016/j.jcp.2011.02.006.

Wood, B. E., H.-R. Muller, G. P. Zank, J. L. Linsky and S. Redfield (2005), New mass-loss measurements from astrospheric Lya absorption, Astrophys. J., 628(August), L143–L146.

Figures

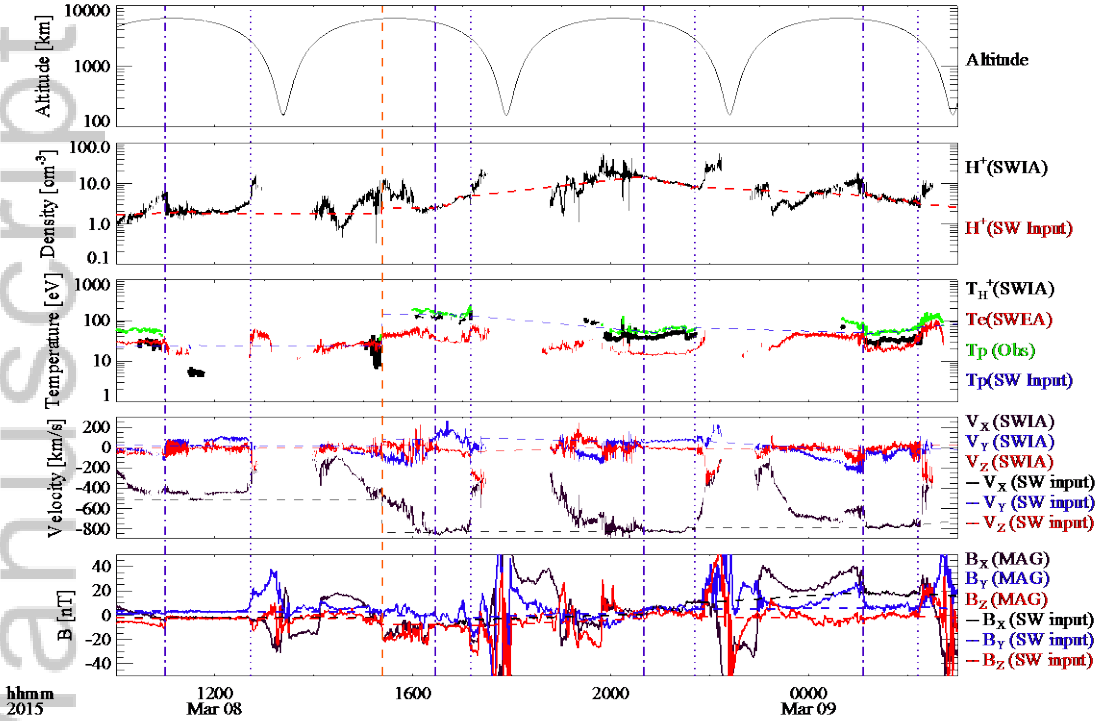

Figure 1: Top panel shows the spacecraft altitude along the trajectory during the ICME event. The rest of the panels shows plasma observations (solid lines) from the SWIA, SWEA and MAG instruments and solar wind input conditions used for the MHD model (dashed lines). The MAVEN bow shock crossings are marked by the dark blue vertical lines: dotted lines for inbound crossings and dash-dotted lines for outbound shock crossings. The orange vertical line marks the time when the ICME leading shock arrived at Mars.

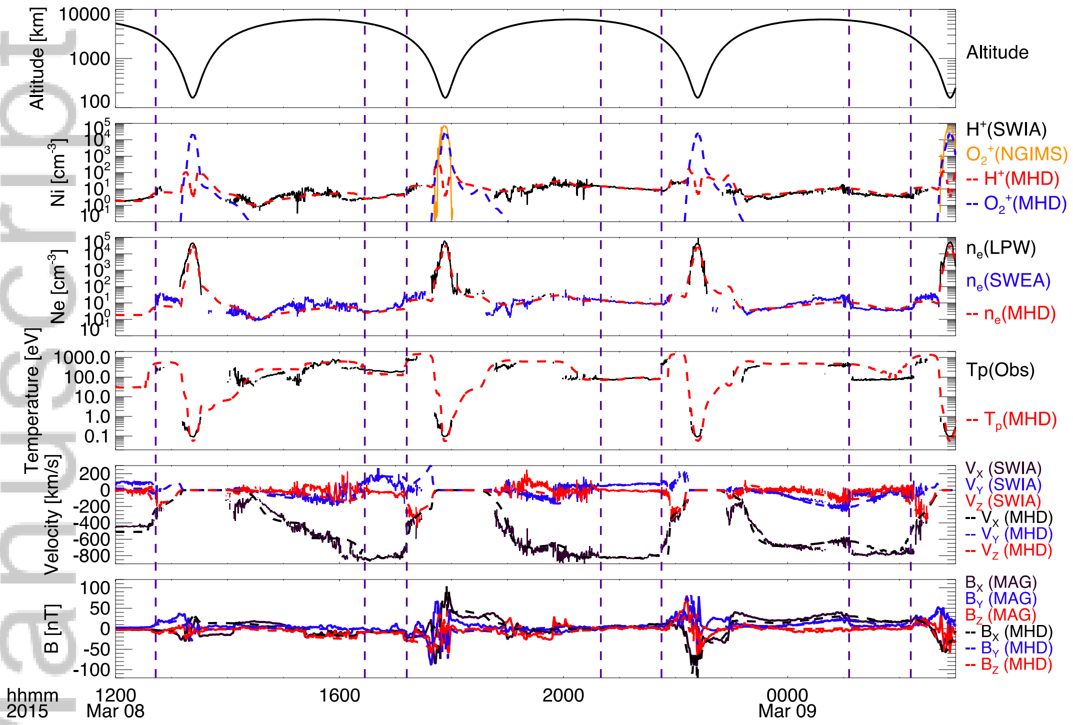

Figure 2: Comparison of the model results with MAVEN plasma observations along the orbit of the spacecraft. Top panel shows the spacecraft altitude along the trajectory; the rest of the panels shows the comparison of ion density, electron density, plasma temperature, velocity and magnetic field between MAVEN observations (solid lines) and MHD model results (dashed lines). T_P(Obs) and T_P(MHD) are the sum of electron temperature and ion temperature based on observation and MHD model results respectively; the observations are based on either LPW and

STATIC near periapsis or SWEA and SWIA in other regions. The bow shock crossings are marked by the dashed dark blue vertical lines.

Time= 15:22 UT

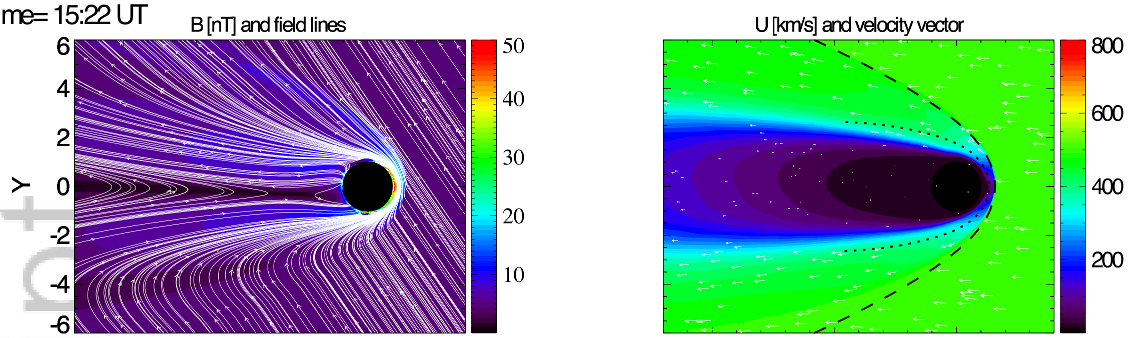

Time= 15:25 UT

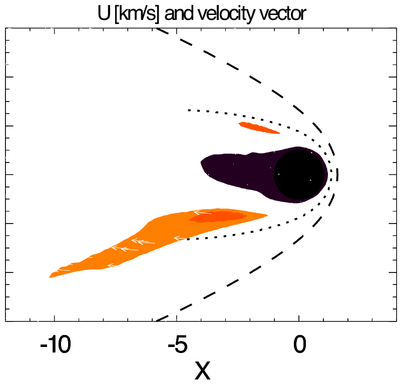

Figure 3. Contour plot of magnetic field strength and field lines (left panels) and plasma flow speed (right panels) in the XY (equatorial) plane at 4 consecutive times starting from 15:22 UT to 15:25 UT, from top to bottom. The mean bow shock and IMB locations are over-plotted on the right panels as references [*Edberg et al*., 2008].

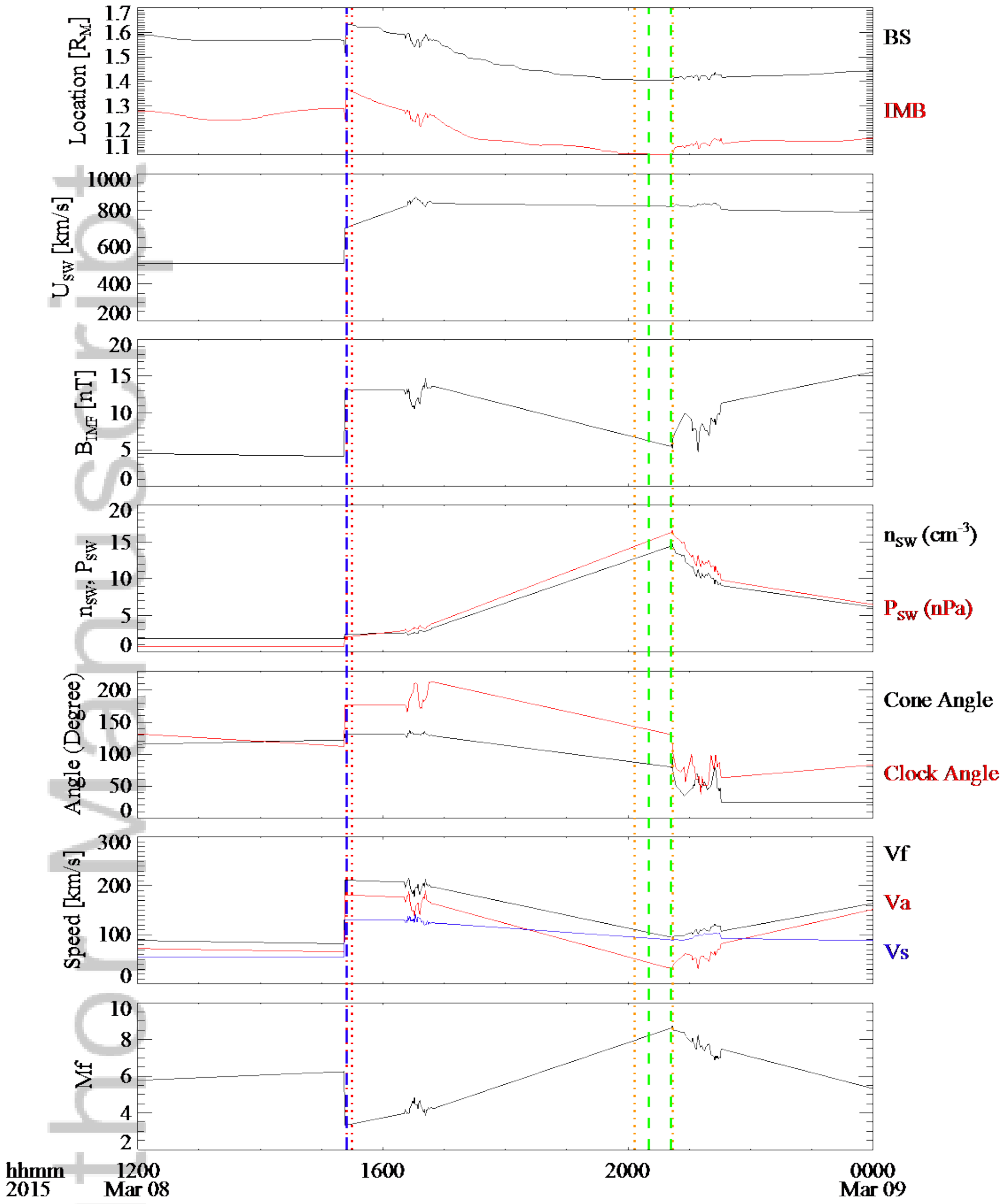
Location [R_M]
1.7
1.6
1.5
1.4
1.3
1.2
1.1
BS
IMB
U_SW [km/s]
1000
800
600
400
200
B_IMF [nT]
20
15
10
5
0
n_SW, P_SW
20
15
10
5
0
n_SW (cm^-3)
P_SW (nPa)
Angle (Degree)
200
150
100
50
0
Cone Angle
Clock Angle
Speed [km/s]
300
200
100
0
Vf
Va
Vs
Mf
10
8
6
4
2
hhmm
2015
1200
Mar 08
1600
2000
0000
Mar 09

Figure 4: Top panel shows the subsolar bow shock (BS) distance and the induced magnetosphere boundary (IMB) location during the ICME event. The second-to-last panels show the solar wind flow speed; IMF strength; solar wind density and pressure; IMF cone angle and clock angle; fast magnetosonic speed, Alfven speed and sonic speed; and fast magnetosonic Mach number, respectively. The cone angle is defined as the $\cos^{-1}(B_X/B)$ and the clock angle is $\tan^{-1}(B_Y/B_Z)$. The time periods when the BS and the IMB were farthest from the planet were between the red and blue dashed lines, respectively. The time periods when BS and IMB were closest to the planet were between the orange and green dashed lines, respectively.

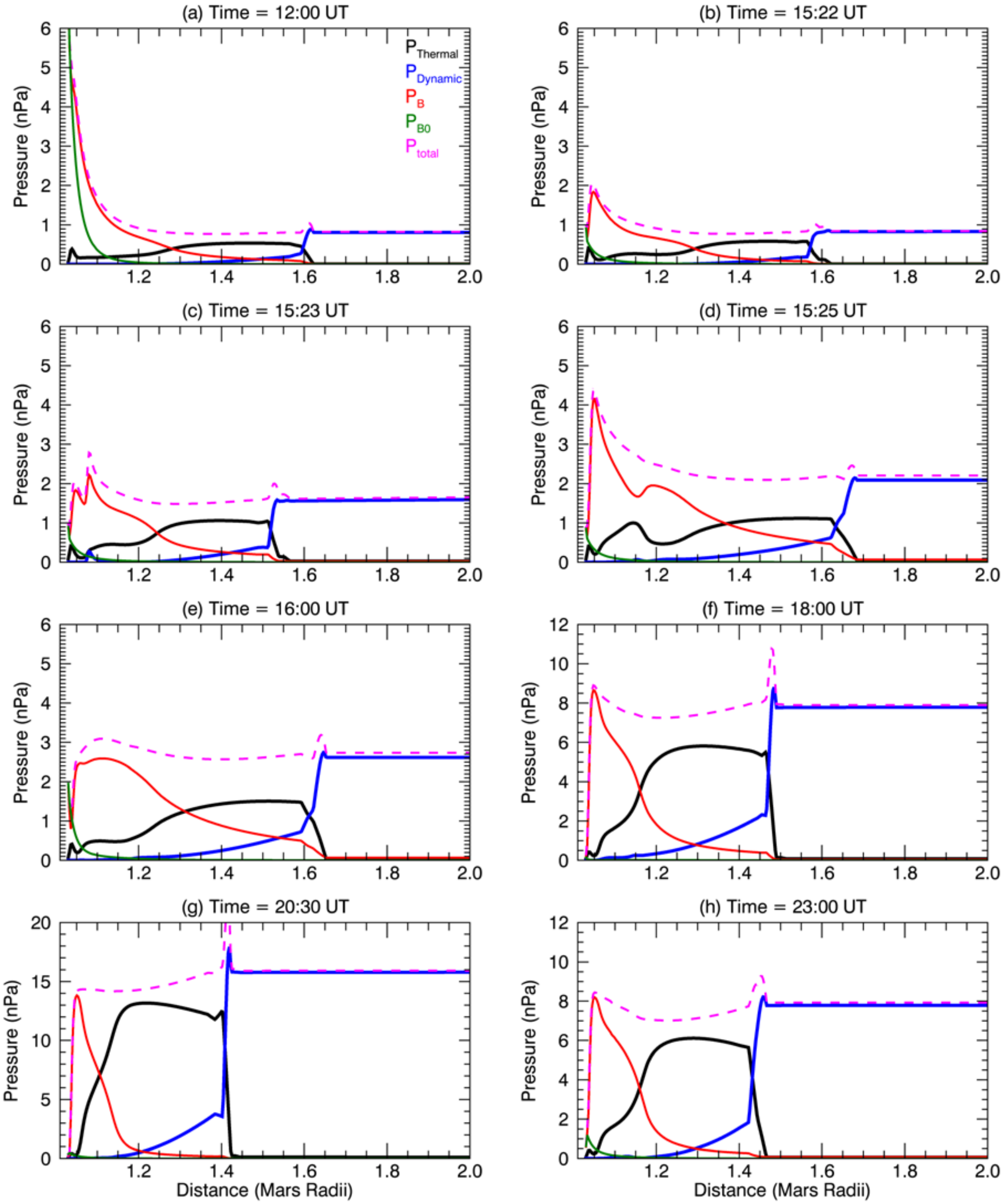
(a) Time = 12:00 UT
(b) Time = 15:22 UT
(c) Time = 15:23 UT
(d) Time = 15:25 UT
(e) Time = 16:00 UT
(f) Time = 18:00 UT
(g) Time = 20:30 UT
(h) Time = 23:00 UT
$P_{Thermal}$
$P_{Dynamic}$
P_B
P_{B0}
P_{total}
Pressure (nPa)
Distance (Mars Radii)
0
1
2
3
4
5
6
8
10
12
15
20
1.2
1.4
1.6
1.8
2.0

Figure 5. Pressure profiles along the Mars-Sun line. Different curves represent different pressures: thermal pressure ($P_{Thermal}$) in black, dynamic pressure ($P_{Dynamic}$ in blue), magnetic pressure (P_B in red), crustal magnetic pressure (P_{B0} in green) and total pressure (P_{total} in purple) at different times. Note the pressure ranges are different for the last three panels.

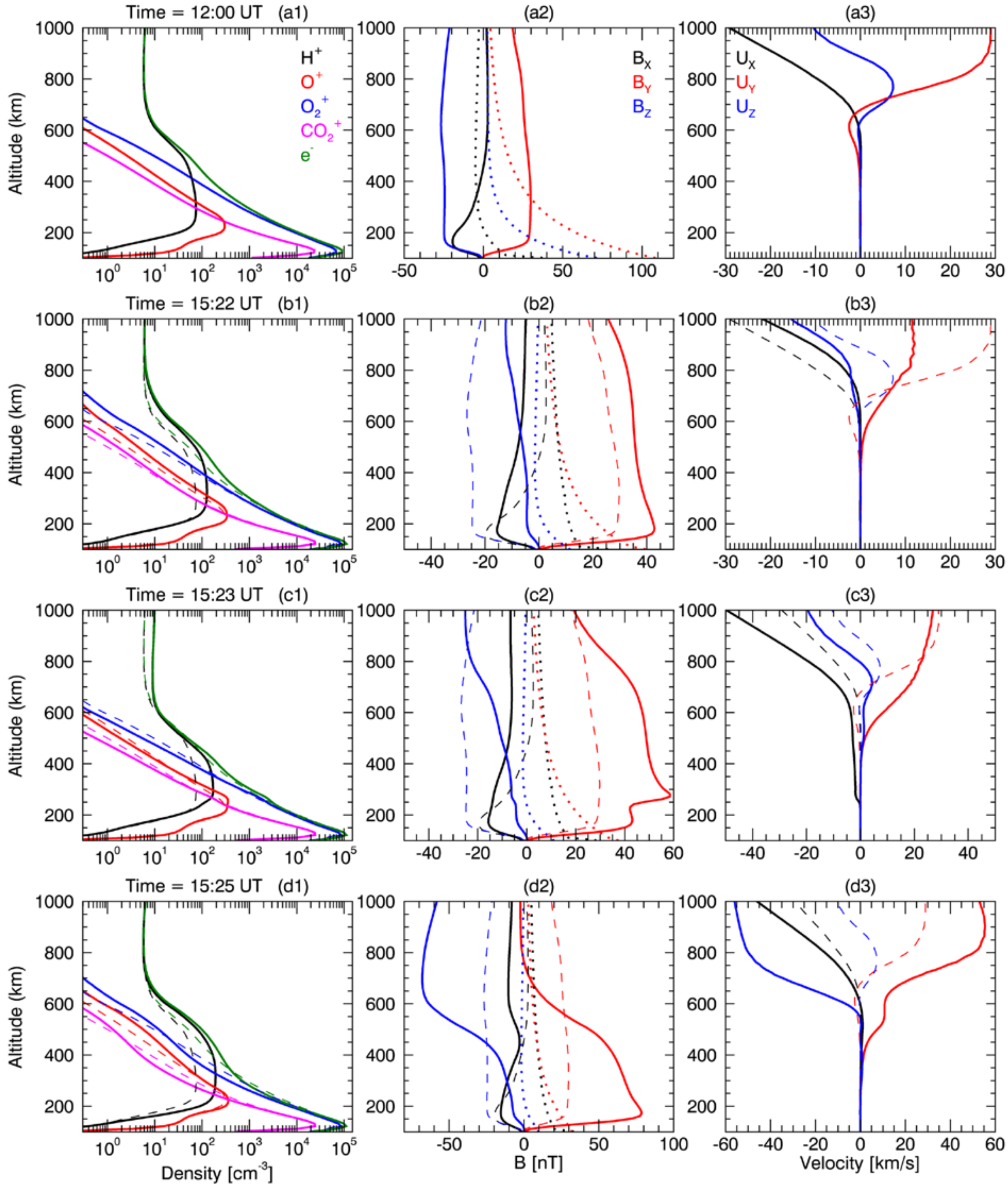
Time = 12:00 UT (a1)
(a2)
(a3)
Time = 15:22 UT (b1)
(b2)
(b3)
Time = 15:23 UT (c1)
(c2)
(c3)
Time = 15:25 UT (d1)
(d2)
(d3)
H^+
O^+
O_2^+
CO_2^+
e^-
B_X
B_Y
B_Z
U_X
U_Y
U_Z
Altitude (km)
Density [cm^{-3}]
B [nT]
Velocity [km/s]
1000
800
600
400
200
10^0 10^1 10^2 10^3 10^4 10^5
-50 0 50 100
-30 -20 -10 0 10 20 30
-40 -20 0 20 40
-40 -20 0 20 40 60
-40 -20 0 20 40
-50 0 50 100
-60 -40 -20 0 20 40 60

Figure 6. Profiles of various plasma properties along the sub-solar line at different times. The left panels show altitude profiles of number densities of different ion species and electrons, and the middle and right panels show altitude profiles of induced magnetic field (solid lines), crustal magnetic field (dotted lines) and velocity components, respectively. The top panels show the results at 12:00 UT. The results in the top panel are over-plotted in dashed lines for the rest of the panels as references. Note that the magnetic field and velocity ranges are different in the figure.

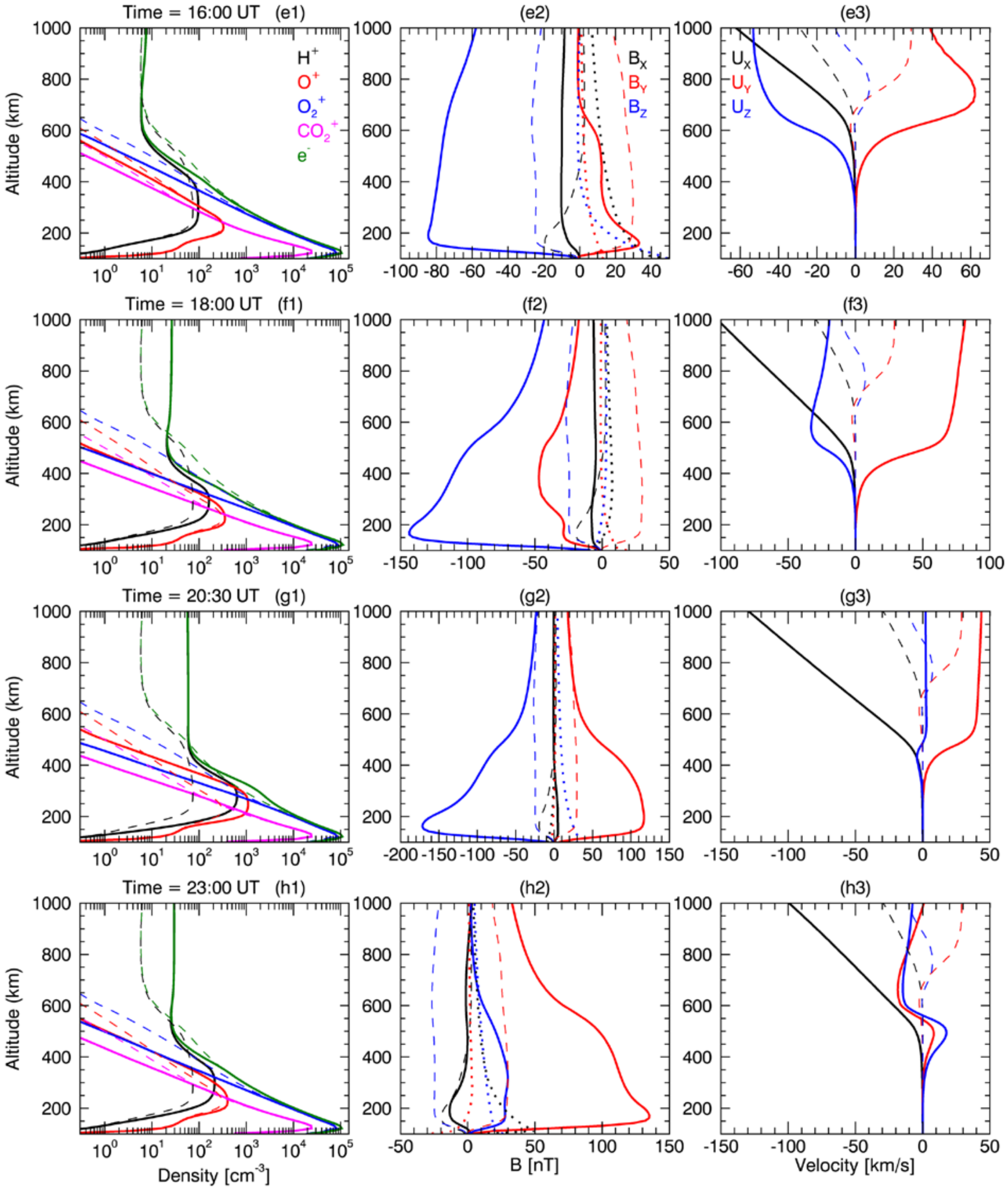
Time = 16:00 UT (e1)
(e2)
(e3)
Time = 18:00 UT (f1)
(f2)
(f3)
Time = 20:30 UT (g1)
(g2)
(g3)
Time = 23:00 UT (h1)
(h2)
(h3)
H^+
O^+
O_2^+
CO_2^+
e^-
B_X
B_Y
B_Z
U_X
U_Y
U_Z
Altitude (km)
1000
800
600
400
200
10^0 10^1 10^2 10^3 10^4 10^5
-100 -80 -60 -40 -20 0 20 40
-60 -40 -20 0 20 40 60
-150 -100 -50 0 50
-100 -50 0 50 100
-200 -150 -100 -50 0 50 100 150
-150 -100 -50 0 50
-50 0 50 100 150
Density [cm^{-3}]
B [nT]
Velocity [km/s]

Figure 6. Continued.

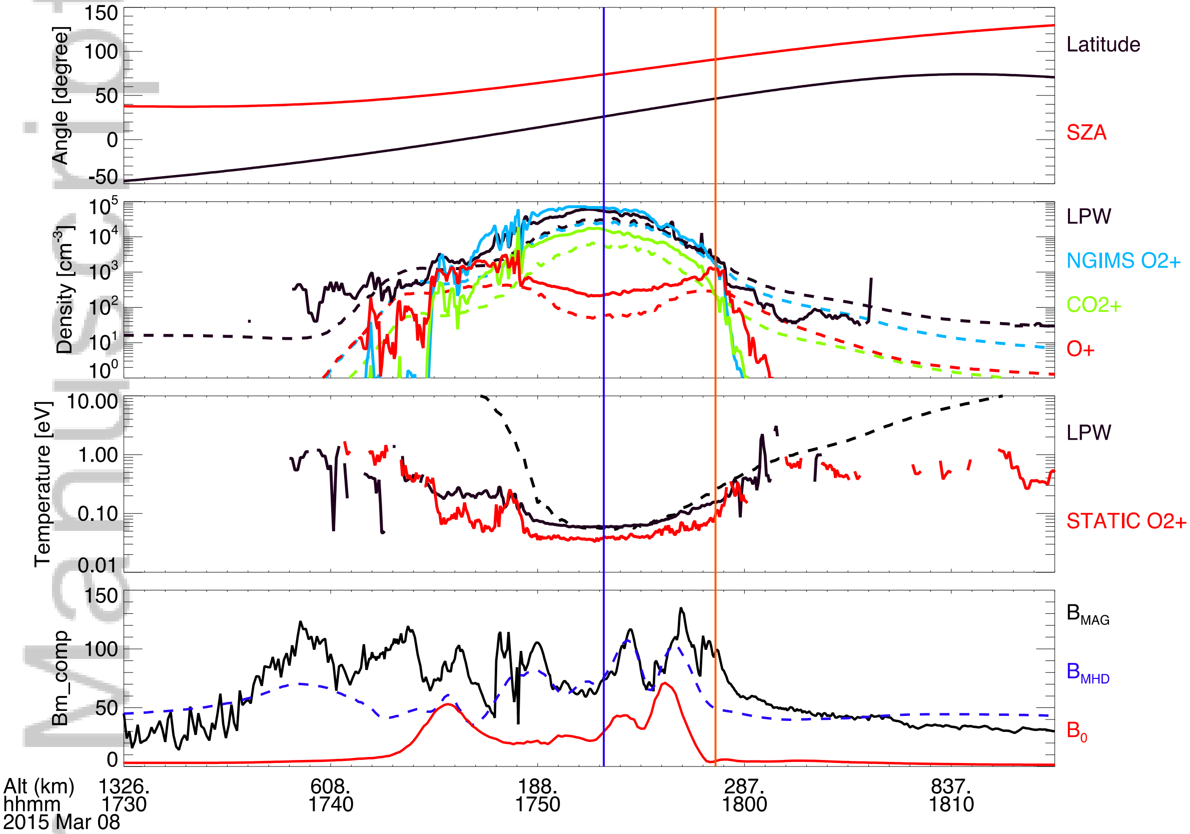

Figure 7. Comparison of model results and MAVEN observations near the periapsis of orbit 848. The solid lines are observations, while the corresponding model results are shown by dashed lines. The top panel shows the latitude and SZA of the spacecraft. The second panel shows electron number density from LPW and ion densities from NGIMS. The third panel shows temperature comparison, and the last panel shows comparison of the magnetic field. The blue

vertical line is the periapsis or closest approach(CA). The orange vertical line is the time when the spacecraft passed the terminator plane (90 degrees SZA).

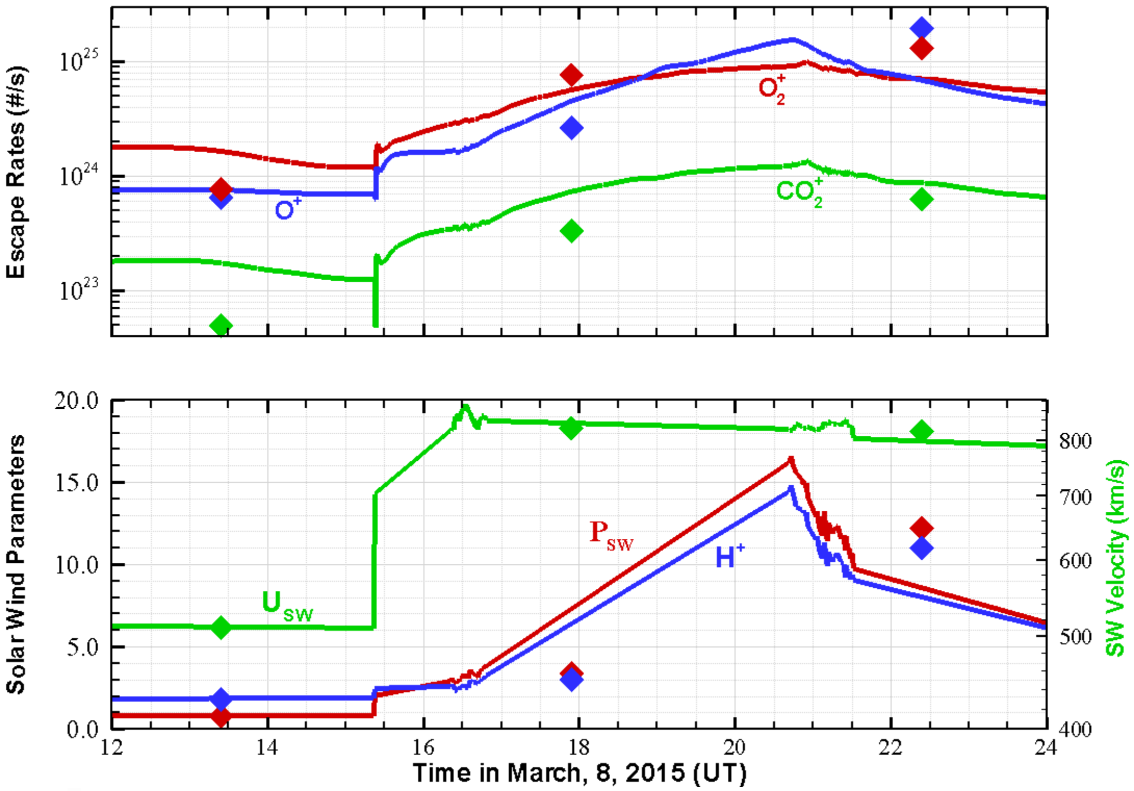

Figure 8. Variation of the modeled ion escape rates and corresponding solar wind conditions. The top panel shows the integrated ion loss rates for O^+ (blue), O_2^+ (red) and CO_2^+ (green). The bottom panel shows solar wind density (blue), velocity (green), and dynamic pressure (red) calculated based on the time-varying solar wind input of the model.

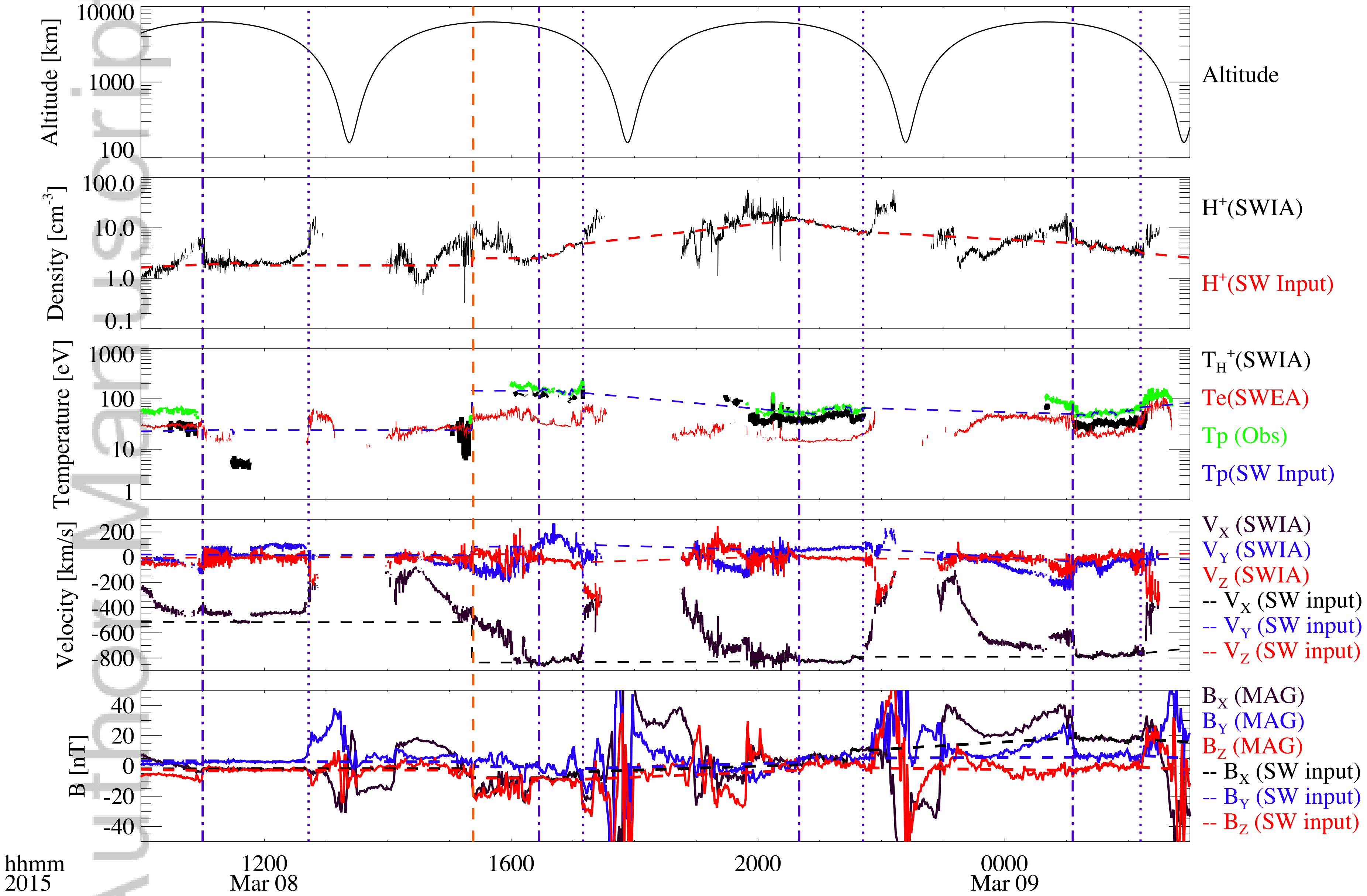
Altitude [km]
10000
1000
100
Altitude
Density [cm^{-3}]
100.0
10.0
1.0
0.1
H$^+$(SWIA)
H$^+$(SW Input)
Temperature [eV]
1000
100
10
1
T_{H^+}(SWIA)
Te(SWEA)
Tp (Obs)
Tp(SW Input)
Velocity [km/s]
200
0
-200
-400
-600
-800
V_X (SWIA)
V_Y (SWIA)
V_Z (SWIA)
-- V_X (SW input)
-- V_Y (SW input)
-- V_Z (SW input)
B [nT]
40
20
0
-20
-40
B_X (MAG)
B_Y (MAG)
B_Z (MAG)
-- B_X (SW input)
-- B_Y (SW input)
-- B_Z (SW input)
hhmm
2015
1200
Mar 08
1600
2000
0000
Mar 09

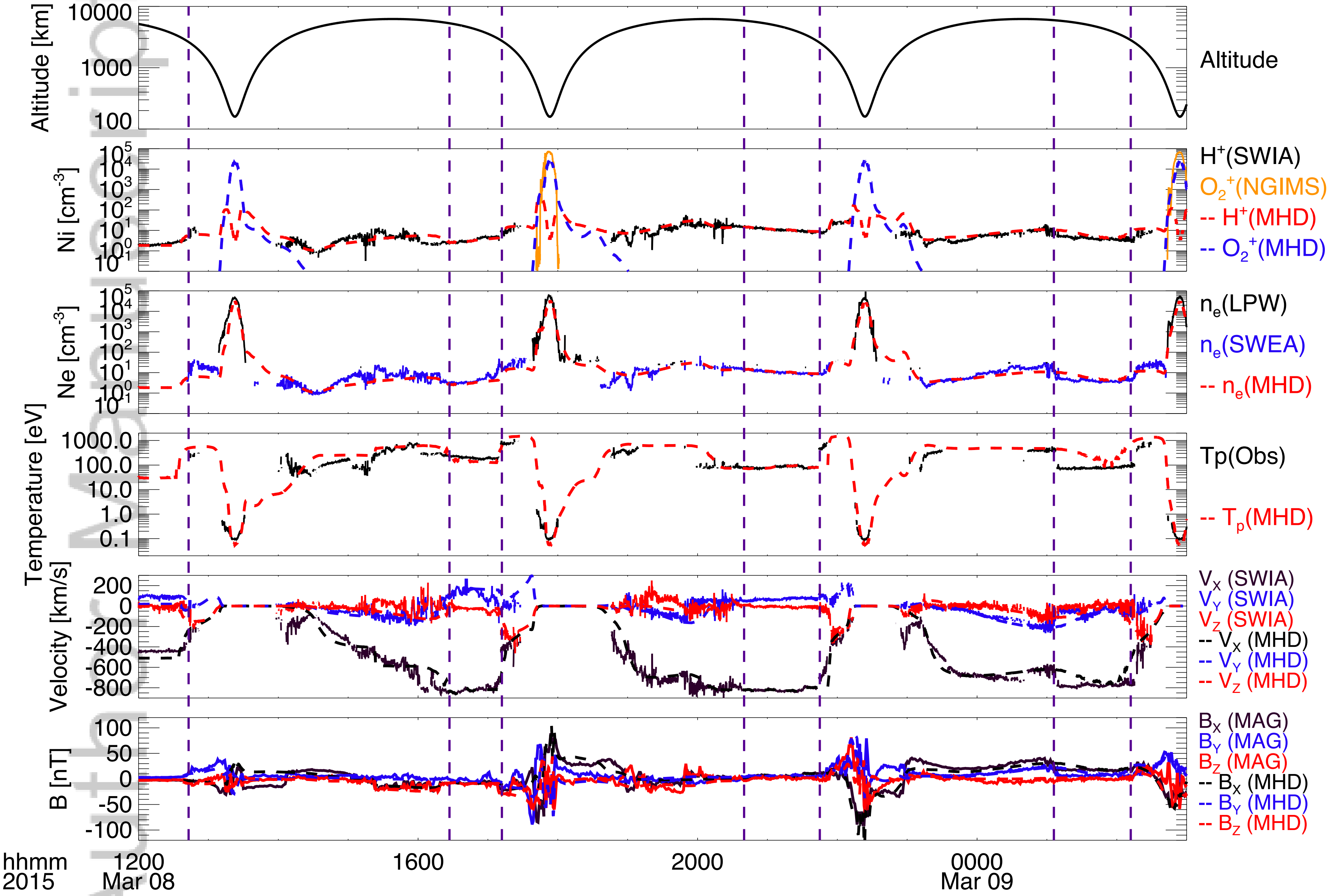
Altitude [km]
10000
1000
100
Altitude
Ni [cm^{-3}]
10^5
10^4
10^3
10^2
10^1
10^0
10^{-1}
H^+(SWIA)
O_2^+(NGIMS)
-- H^+(MHD)
-- O_2^+(MHD)
Ne [cm^{-3}]
n_e(LPW)
n_e(SWEA)
-- n_e(MHD)
Temperature [eV]
1000.0
100.0
10.0
1.0
0.1
Tp(Obs)
-- T_p(MHD)
Velocity [km/s]
200
0
-200
-400
-600
-800
V_X (SWIA)
V_Y (SWIA)
V_Z (SWIA)
-- V_X (MHD)
-- V_Y (MHD)
-- V_Z (MHD)
B [nT]
100
50
0
-50
-100
B_X (MAG)
B_Y (MAG)
B_Z (MAG)
-- B_X (MHD)
-- B_Y (MHD)
-- B_Z (MHD)
hhmm
2015
1200
Mar 08
1600
2000
0000
Mar 09

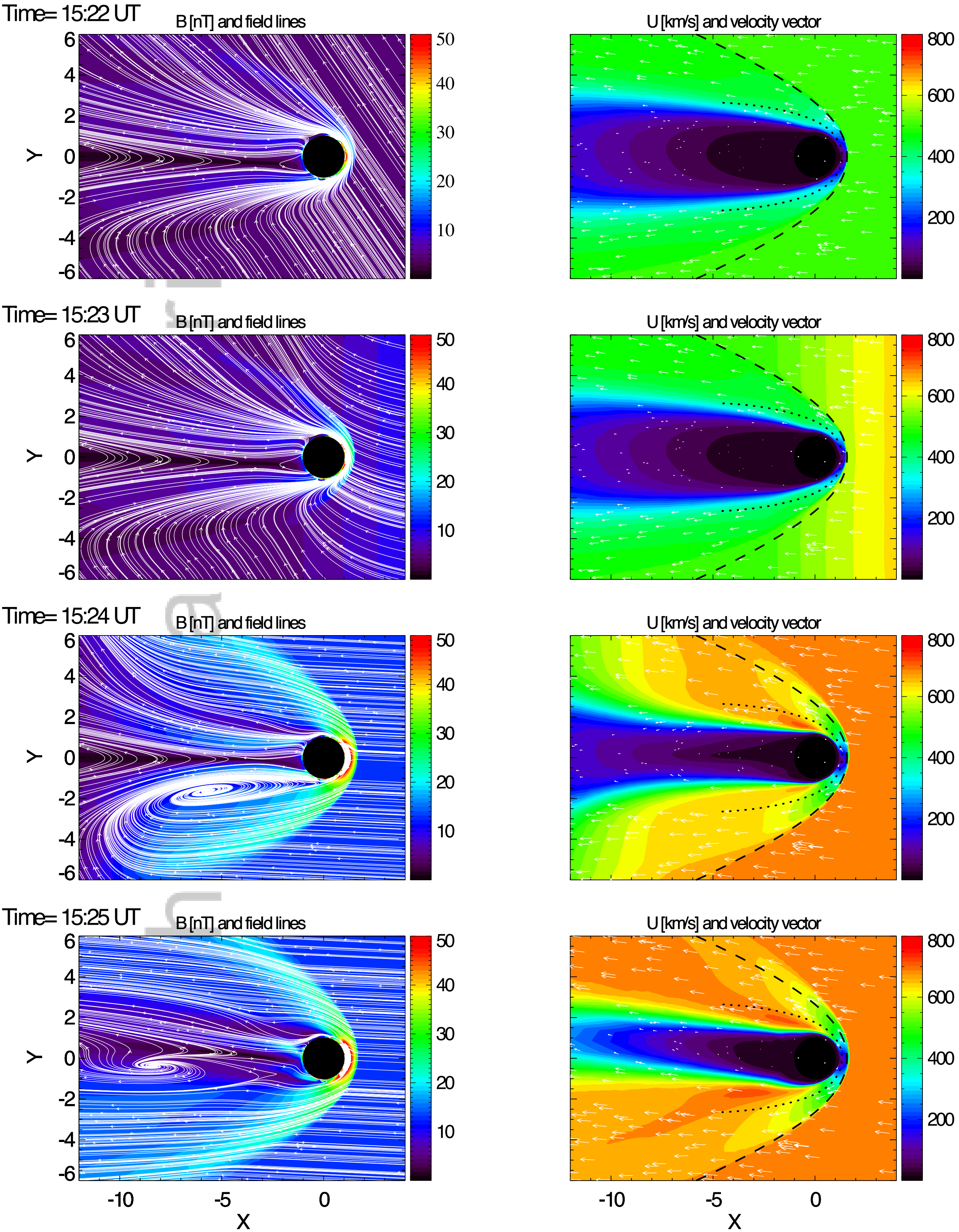
Time= 15:22 UT
B [nT] and field lines
U [km/s] and velocity vector
Time= 15:23 UT
B [nT] and field lines
U [km/s] and velocity vector
Time= 15:24 UT
B [nT] and field lines
U [km/s] and velocity vector
Time= 15:25 UT
B [nT] and field lines
U [km/s] and velocity vector
Y
6
4
2
0
-2
-4
-6
10
20
30
40
50
200
400
600
800
-10
-5
0
X

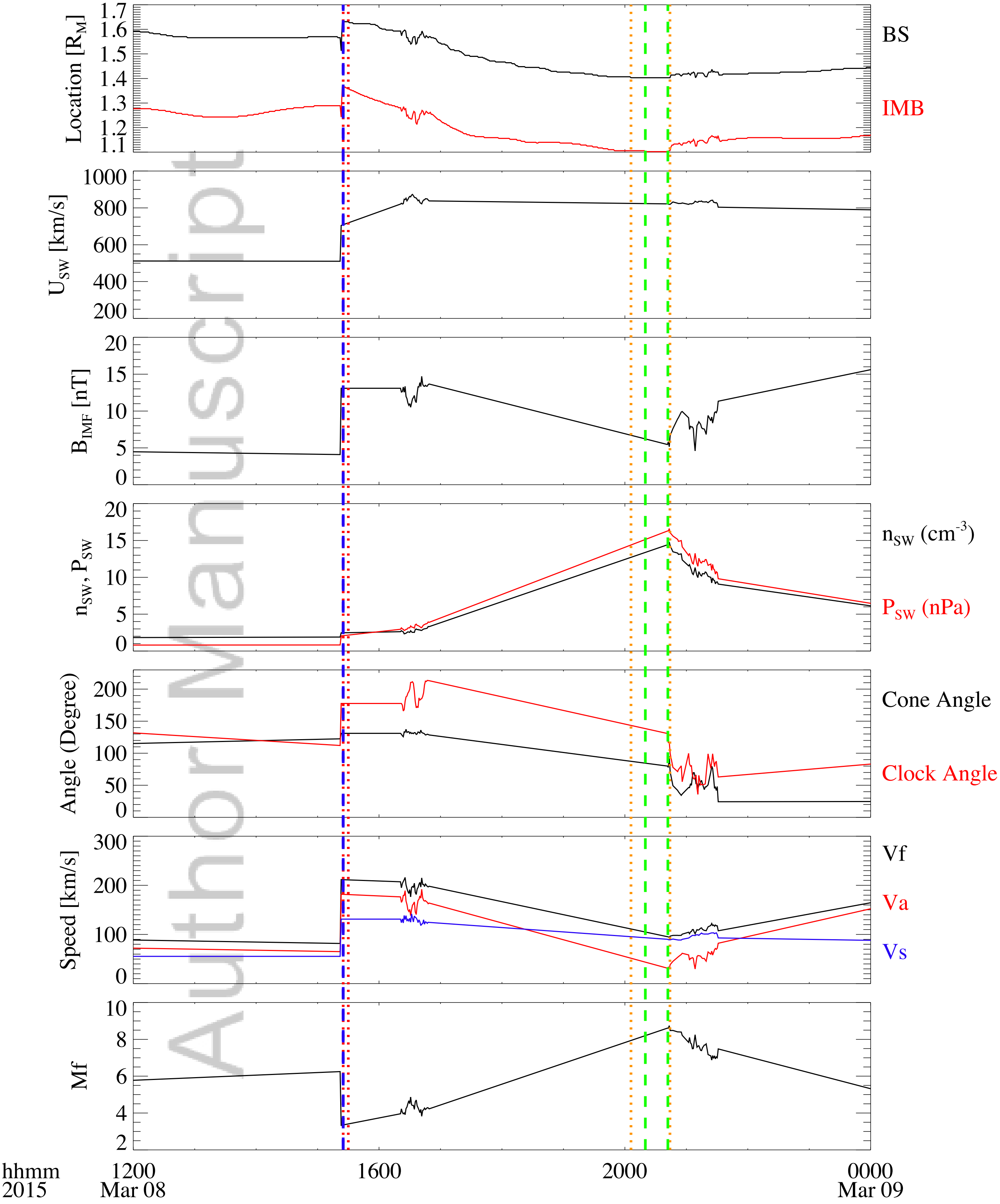
Location [R$_M$]
1.7
1.6
1.5
1.4
1.3
1.2
1.1
BS
IMB
U$_{SW}$ [km/s]
1000
800
600
400
200
B$_{IMF}$ [nT]
20
15
10
5
0
n$_{SW}$, P$_{SW}$
n$_{SW}$ (cm^{-3})
P$_{SW}$ (nPa)
Angle (Degree)
200
150
100
50
0
Cone Angle
Clock Angle
Speed [km/s]
300
200
100
0
Vf
Va
Vs
Mf
10
8
6
4
2
hhmm
2015
1200
Mar 08
1600
2000
0000
Mar 09

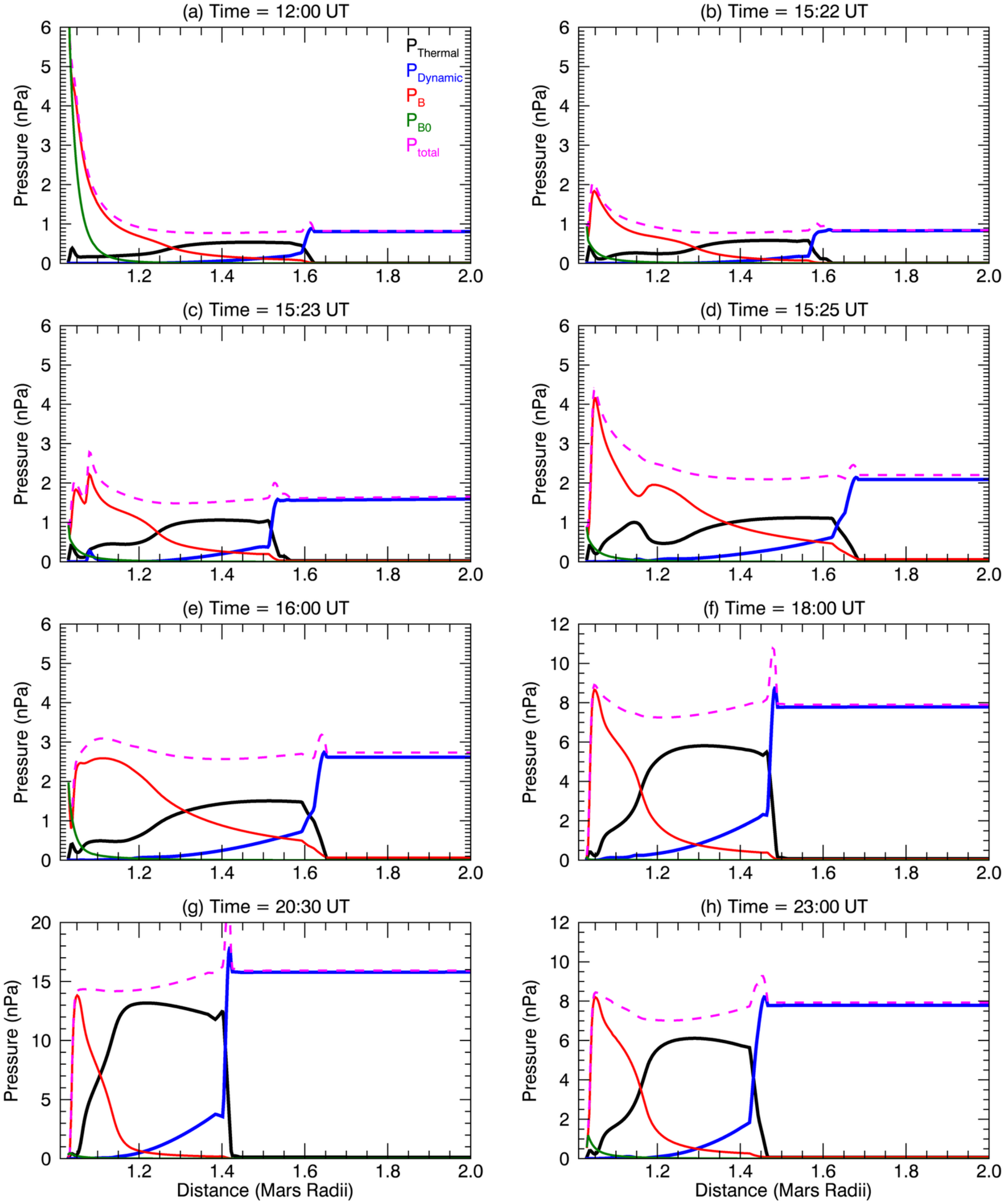

2016JA023402-f05-z-.png

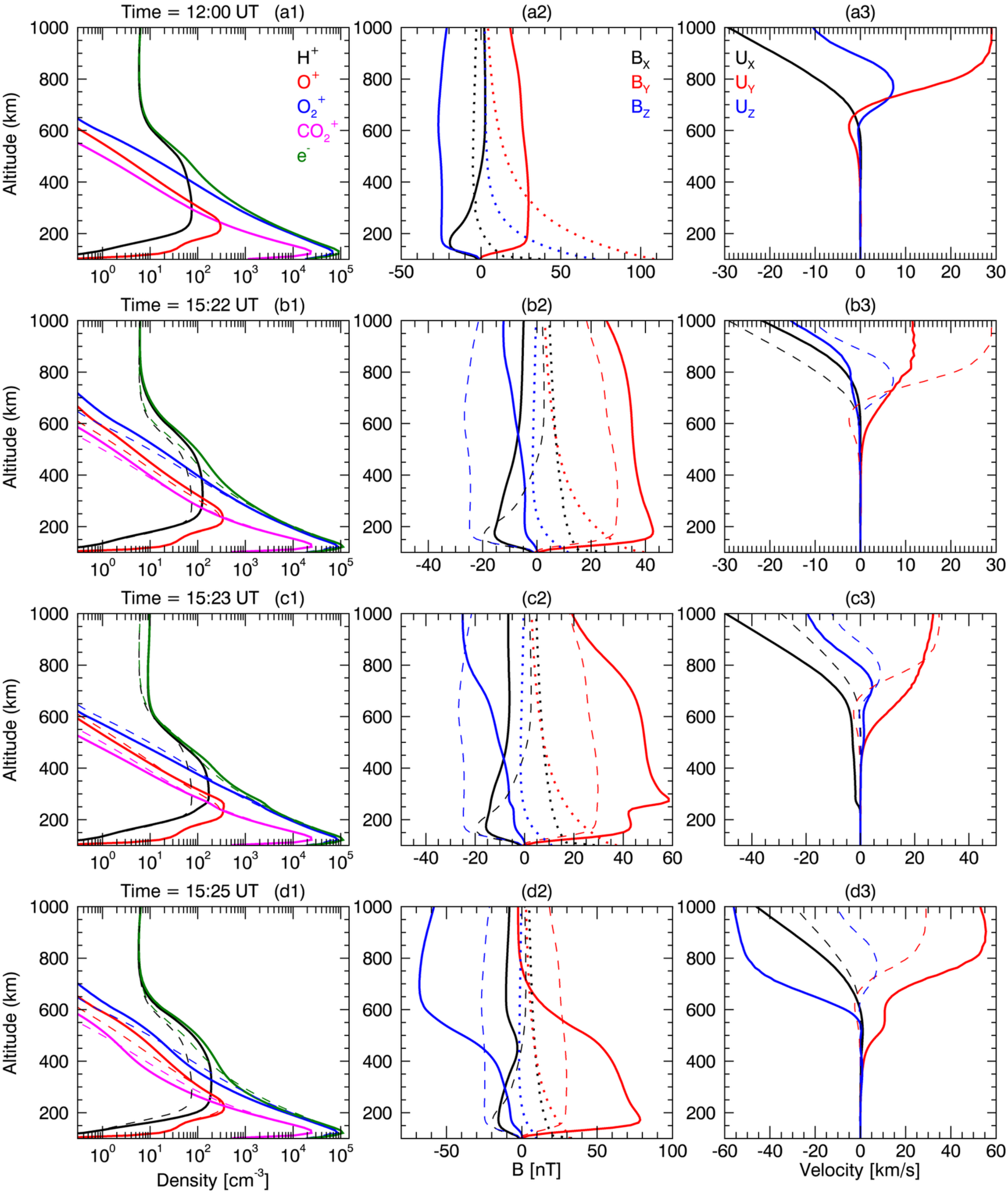

2016JA023402-f06-z-.png

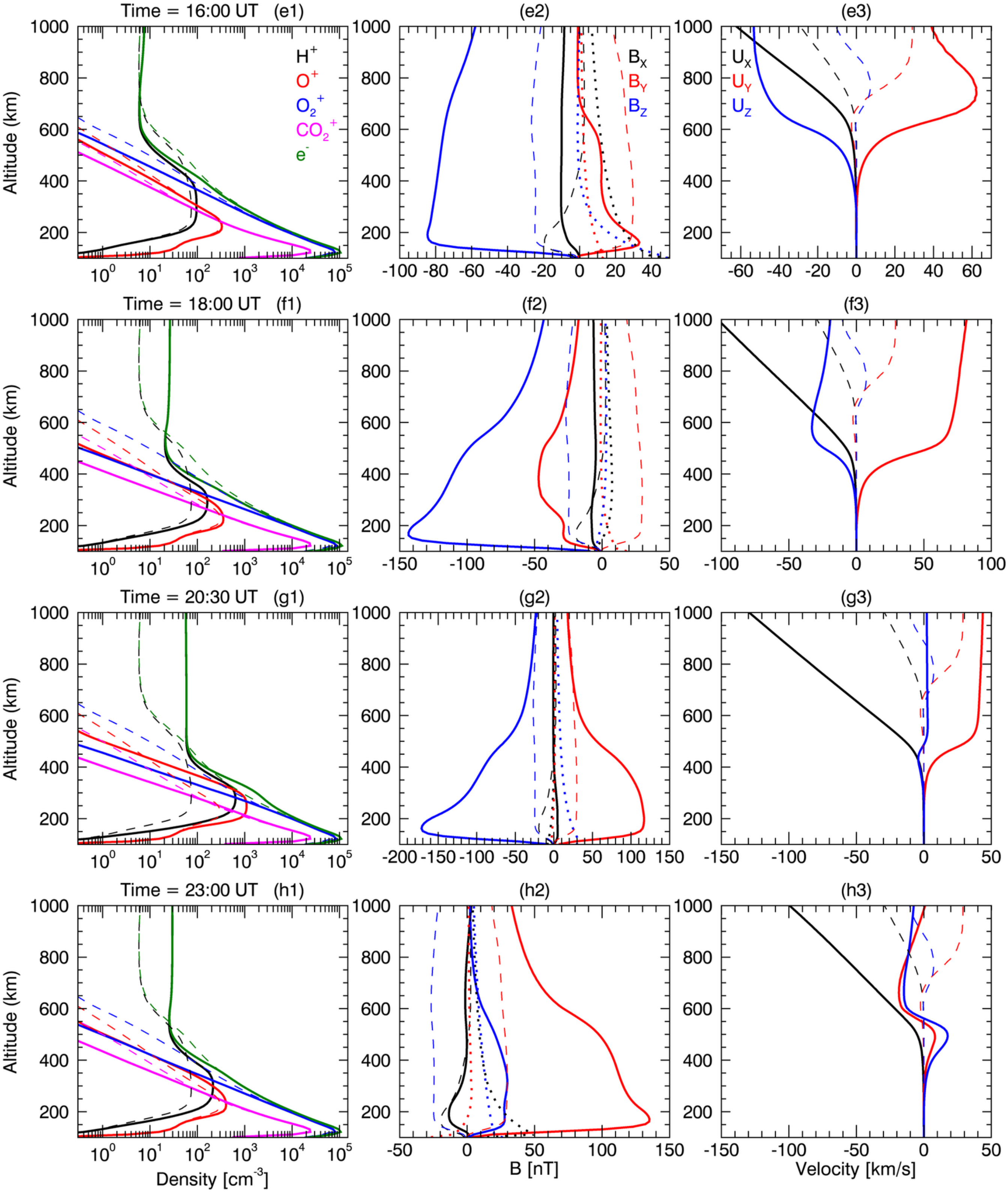

2016JA023402-f07-z-.png

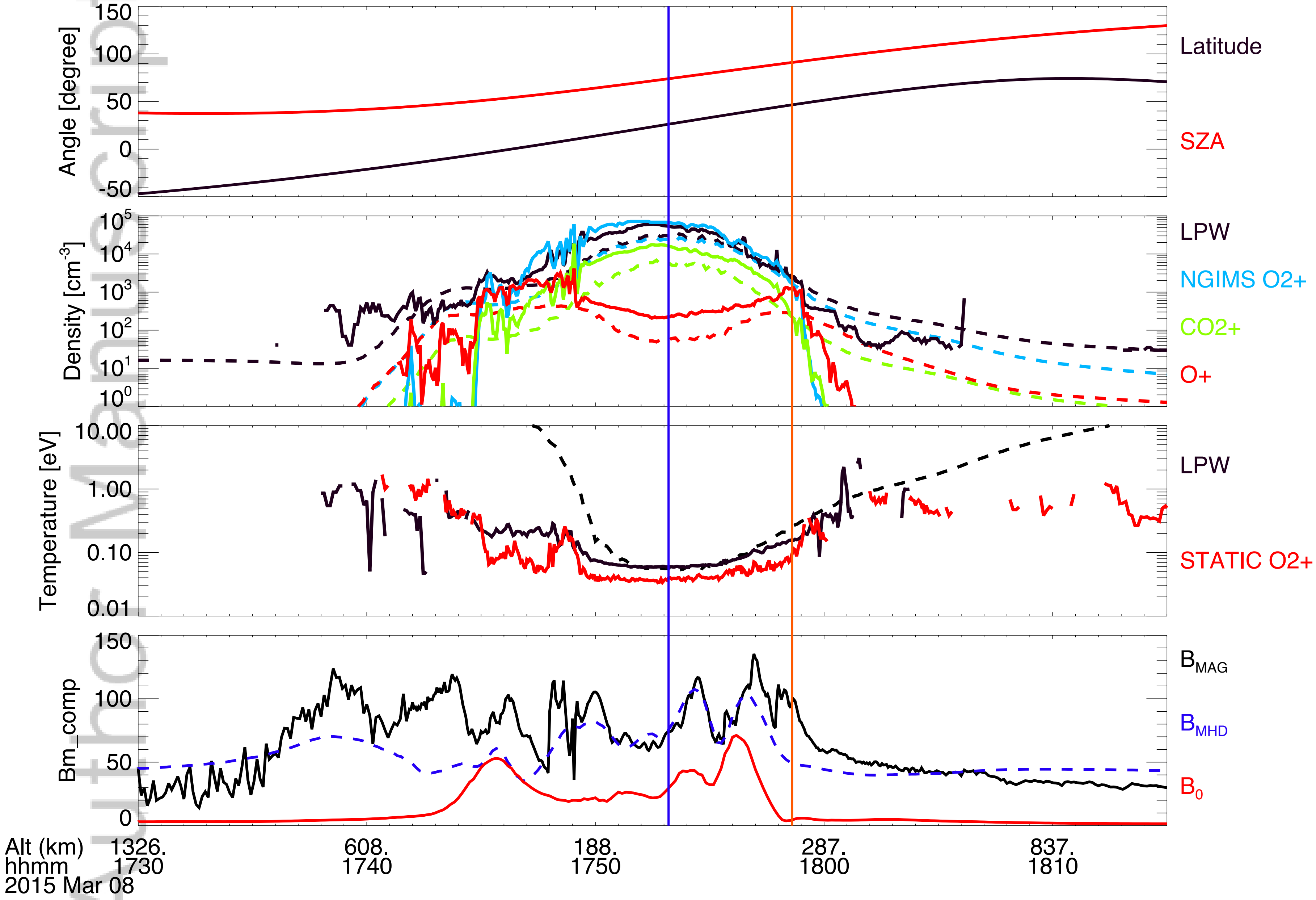
Angle [degree]
150
100
50
0
-50
Latitude
SZA
Density [cm^{-3}]
10^5
10^4
10^3
10^2
10^1
10^0
LPW
NGIMS O2+
CO2+
O+
Temperature [eV]
10.00
1.00
0.10
0.01
LPW
STATIC O2+
Bm_comp
150
100
50
0
B_{MAG}
B_{MHD}
B_0
Alt (km)
hhmm
2015 Mar 08
1326.
1730
608.
1740
188.
1750
287.
1800
837.
1810

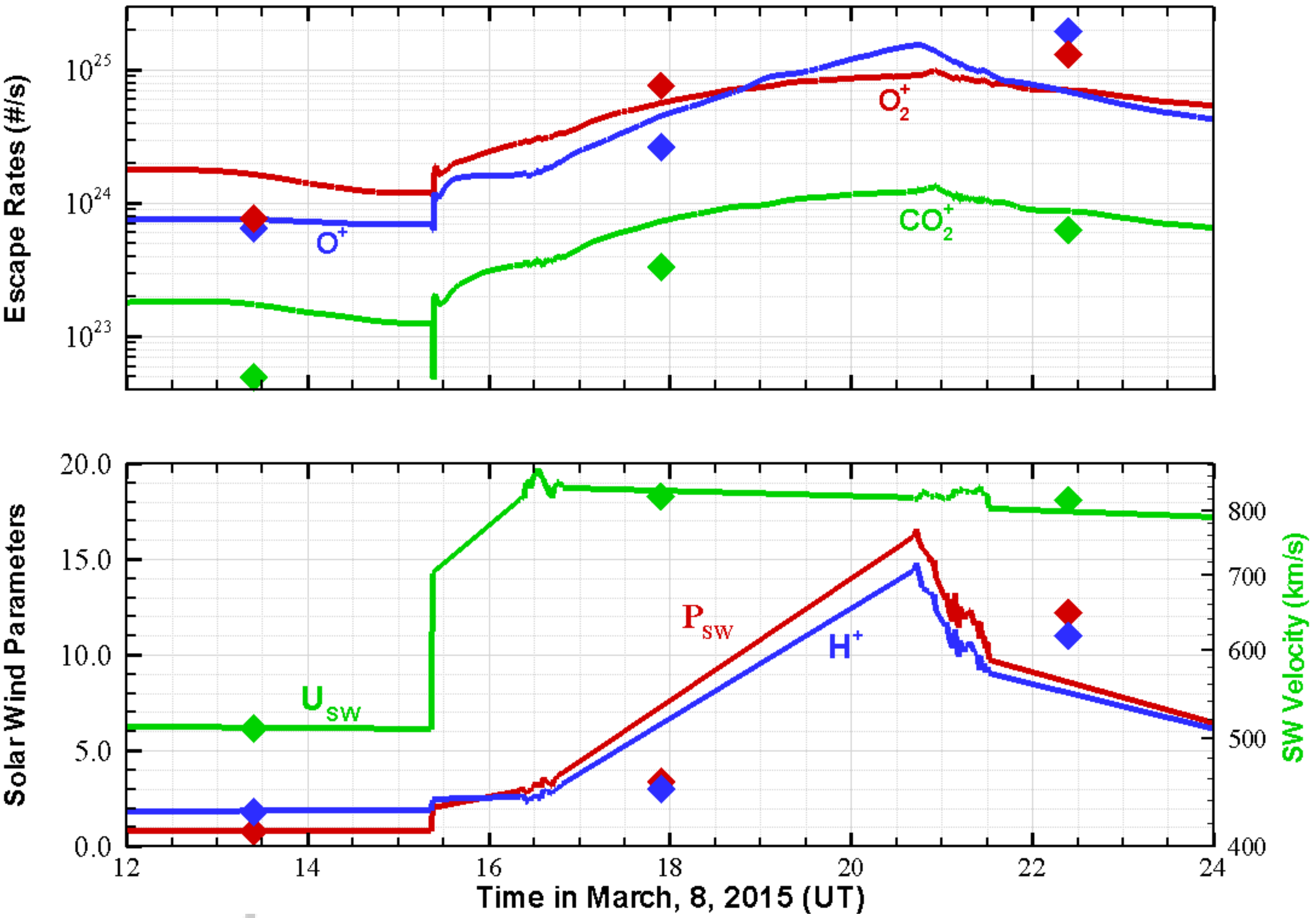

2016JA023402-f09-z-.tif